Deformation of a compliant wall in a turbulent channel flow

Cao Zhang[1], **Jin Wang**[1], **William Blake**[1] **and Joseph Katz**[1,†]

[1]Department of Mechanical Engineering, Johns Hopkins University, Baltimore, MD 21218, USA

Interaction of a compliant wall with a turbulent channel flow is investigated experimentally by simultaneously measuring the time-resolved, three-dimensional (3D) flow field and the two-dimensional (2D) surface deformation. The optical set-up integrates tomographic particle image velocimetry to measure the flow with Mach–Zehnder interferometry to map the deformation. The Reynolds number is $Re_\tau = 2300$, and the Young's modulus of the wall is 0.93 MPa, resulting in a ratio of shear speed to the centreline velocity (U_0) of 6.8. The wavenumber–frequency spectra of deformation show the surface motions consist of a non-advected low-frequency component and advected modes, some travelling downstream at approximately U_0 and others at $\sim 0.72U_0$. The r.m.s. values of the advected and non-advected modes are 0.04 μm ($0.004\delta_\nu$) and 0.2 μm ($0.02\delta_\nu$), respectively, much smaller than the wall unit (δ_ν), hence they do not affect the flow. Trends in the wall dynamics are elucidated by correlating the deformation with flow variables, including the 3D pressure distribution calculated by spatially integrating the material acceleration. Predictions by the Chase [*J. Acoust. Soc. Am.*, vol. 89 (6), pp. 2589–2596] linear model are also calculated and compared to the measured trends. The spatial deformation–pressure correlations peak at $y/h \approx 0.12$ (h is half channel height), the elevation of Reynolds shear stress maximum in the log-layer. Streamwise lagging of the deformation behind the pressure is caused in part by phase lag of the pressure with decreasing distance from the wall, and in part by material damping. Positive deformations (bumps) caused by negative pressure fluctuations are preferentially associated with ejections involving spanwise vortices located downstream and quasi-streamwise vortices with spanwise offset. Results of conditional correlations are consistent with the presence of hairpin-like structures. The negative deformations (dimples) are preferentially associated with positive pressure fluctuations at the transition between an upstream sweep to a downstream ejection.

Key words: turbulent boundary layers, turbulent flows

1. Introduction

The interactions between compliant surfaces and laminar or turbulent boundary layers have been the subject of numerous investigations over the past 60 years owing to their presumed effects on laminar to turbulent transition, skin friction, as well as

† Email address for correspondence: katz@jhu.edu

noise and vibrations (Bushnell, Hefner & Ash 1977; Riley, Gad-el-Hak & Metcalfe 1988; Gad-el-Hak 1998, 2002). Early studies were stimulated by Kramer (1957, 1962), who reported considerable drag reduction by coating a model with a compliant surface mimicking the skin of dolphins. Subsequent experimental investigations showed mixed results, namely some observed drag reduction (e.g. Fisher & Blick 1966; Blick & Walters 1968; Choi *et al.* 1997), but others did not (e.g. Harris & Lissaman 1969; McMichael, Klebanoff & Mease 1980). In efforts aimed at explaining the mechanisms involved, the theoretical works of Benjamin (1960, 1963) and Landahl (1962) suggested that by selecting the flexibility and internal damping of the material, the compliant surface could delay the transition from laminar to turbulent flow. The choice of material properties was critical because the wall compliance could also allow other instability modes to grow and trigger transition.

Many subsequent studies investigated the effect of a compliant surface on boundary layer transition. For example, the theoretical analysis of Carpenter & Garrad (1985, 1986) divided the flow instability into two categories, namely Tollmien–Schlichting (TS) type instabilities resembling those occurring over a rigid plate, and flow-induced surface instabilities (FISI). The TS waves were stabilized by the wall compliance and destabilized by material damping. The FISI, on the other hand, were destabilized by wall compliance and stabilized by material damping. Lee, Fisher & Schwarz (1995) studied the effect of a compliant surface on the stability of the Blasius boundary layer in a wind tunnel. They confirmed that at low Reynolds numbers, when the amplitudes of FISI were small, the wall compliance reduced the growth rate of unstable TS waves. Wang, Yeo & Khoo (2006) reached the same conclusion based on direct numerical simulation (DNS). Another research direction focused at the interactions between the compliant surface and fully developed turbulent boundary layers. For soft materials, experimental studies revealed the formation of the so-called static-divergence wave (Hansen & Hunston 1974; Hansen *et al.* 1980; Hansen & Hunston 1983; Gad-el-Hak, Blackwelder & Riley 1984). The crests of these waves were aligned in the spanwise direction, and they exhibited low phase speeds ($\sim 0.05 U_0$) and high amplitudes of the order of the coating thickness. They appeared when the free-stream velocity was several times larger than the shear wave speed of the compliant coating, c_t. Formation of such waves usually increased the drag, presumably due to an increase in surface roughness (Hansen & Hunston 1974; Gad-el-Hak *et al.* 1984). In the absence of static-divergence waves at speeds lower than the onset level, the tools available to Gad-el-Hak *et al.* (1984) could not detect measurable surface deformation or changes to the mean velocity profile.

The wall deformation detection techniques have improved over the years. Starting with point measurements, Gad-el-Hak *et al.* (1984), Gad-el-Hak (1986) and Hess, Peattie & Schwarz (1993) achieved resolutions of approximately 20 µm and 2 µm, respectively. They illuminated the compliant surface with a laser beam and recorded the displacement of the light scattered from the interface using magnified imaging. In recent years, the introduction of a laser Doppler vibrometer (LDV) allowed point measurement of surface motion at a nanometre precision (e.g. Castellini, Martarelli & Tomasini 2006; Tabatabai *et al.* 2013). Two-dimensional distributions of compliant surface deformations were measured first by Lee, Fisher & Schwarz (1993a,b) using holographic interferometry. They achieved a sub-micron precision, but having to record the interferograms on films, the data was not time-resolved. Yet, they captured 3D small-amplitude deformation patterns that were different from the static-divergence waves. Since the previous experimental studies did not involve simultaneous measurements of flow field and deformation, interactions

could only be inferred based on integrated statistics of mean flow, skin friction and turbulence parameters. To address this challenge, in Zhang, Miorini & Katz (2015), we introduced a system capable of measuring the time-resolved 3D flow and 2D deformation simultaneously. It was used for obtaining the data presented in this paper, and discussed in detail in the following sections.

Over the past two decades, numerical simulations of interactions of a boundary layer with modelled surface compliance have taken a leading role as a research tool (e.g. Endo & Himeno 2002; Xu, Rempfer & Lumley 2003; Kim & Choi 2014; Luhar, Sharma & McKeon 2015). DNS of a turbulent channel flow ($Re_\tau = u_\tau h/\nu = 150$, where u_τ is the friction velocity, h is the channel half-height and ν is the liquid kinematic viscosity) over a soft compliant wall modelled as an array of springs and dampers by Endo & Himeno (2002) showed a moderate reduction (2.7 %) of the average drag. A subsequent investigation by Xu *et al.* (2003) at $Re_\tau = 137$, which modelled the wall in a similar manner, found little change in the averaged skin friction. Simulations by Kim & Choi (2014) at $Re_\tau = 138$ concluded that for a soft wall, large-amplitude quasi-2D surface waves form and travel downstream at a phase speed of less than 40 % of the centreline velocity. Their amplitude and shape were consistent with those of the static-divergence waves, but their celerity was higher. For stiffer walls, their deformation patterns became more complex, and travelled at 72 % of the centreline velocity. In both cases, there was no drag reduction. Luhar *et al.* (2015) used a reduced-order model based on the resolvent analysis introduced by McKeon & Sharma (2010) for the flow and modelled the compliant wall effect using a boundary with complex admittance. They showed that an unphysical negative material damping was required for the compliant surface to interact favourably in terms of Reynolds stress distributions with the near-wall motions. Positive damping was only effective for modes representing very-large-scale motions. In parallel, substantial effort was invested in modelling, computing and measuring the response of compliant walls to pressure and shear perturbations (e.g. Duncan, Waxman & Tulin 1985; Duncan 1986; Ko & Schloemer 1989; Chase 1991). These studies focused on the material dynamics, and did not involve flow simulations. Yet, they provided considerable insight on effects of layer thickness and material properties, such as the Young and shear moduli as well as the so-called loss tangent, on the response of the wall to prescribed forcing. The Helmholtz-equation-based analysis by Chase (1991) was particularly relevant to the present study, and was instrumental for elucidating many of the observations. Hence, it is summarized briefly in appendix A.

As a general observation, the mechanisms dominating the compliant wall–flow interactions in high-Reynolds-number turbulent boundary layers have not been elucidated yet. The experimental studies could not resolve them, and even the most recent computational investigations replaced the wall with simplified models. To advance the state of knowledge, in Zhang *et al.* (2015), we integrated time-resolved tomographic particle image velocimetry (TPIV) for measuring the flow (Elsinga *et al.* 2006; Scarano 2013) and Mach–Zehnder interferometry (MZI) (e.g. Hecht 2002) for mapping the corresponding 2D distribution of compliant wall deformation. Section 2 briefly describes the experimental set-up, measurement procedures and uncertainties. For the present analysis, we also calculated the 3D pressure distribution by spatially integrating the material acceleration (Liu & Katz 2006, 2008, 2013; Joshi, Liu & Katz 2014). A brief summary of the GPU-based procedure is provided in appendix B. Other approaches for calculating the pressure based on solutions to the Poisson equation were presented in, for example, Baur & Köngeter (1999), Gurka *et al.* (1999), Koschatzky *et al.* (2011), Ghaemi, Ragni & Scarano (2012), de Kat & van

Oudheusden (2012) and Ghaemi & Scarano (2013), and compared by Charonko *et al.* (2010). Utilizing these techniques, our objective is to investigate how the flow and pressure fields affect the surface deformation in a channel flow at moderately high Reynolds number. The current wall is stiffer than those previously tested in studies attempting to reduce the wall friction, resulting in surface deformations that do not involve static-divergence waves.

Section 3 presents the main findings of this paper. First, the dynamics of pressure and surface deformation are characterized in the frequency domain and by examining their wavenumber–frequency spectra. Based on the results, the deformation is divided into advected and non-advected modes, and most of the subsequent analysis focuses on the latter. Conditional sampling and correlations involving the distributions of deformation, pressure, as well as velocity and vorticity components are used for identifying key flow phenomena affecting the advected modes. This conditional analysis identifies flow structures associated with positive (bumps) and negative (dimples) surface deformations. It also shows that dominant flow features affecting the deformation reside in the log-layer. Causes for phase lag between, for example, pressure and deformation peaks are elucidated based on the material properties and spatial characteristics of near-wall turbulence. Concluding remarks along with conceptual models identifying the dominant flow structures and their spatial relationship with the deformation fields are summarized in §4.

2. Facility, experimental set-up and measurement procedures

2.1. *Test facility*

The experiments have been performed in an acrylic channel extended from the optically index-matched facility at Johns Hopkins University. Detailed descriptions of this channel are documented in several previous publications (Hong, Katz & Schultz 2011; Hong *et al.* 2012; Talapatra & Katz 2012, 2013; Joshi *et al.* 2014; Zhang *et al.* 2015). Figure 1 is a sketch of the relevant parts of the channel extension drawn not to scale. Its overall internal dimensions are $3300 \times 50.8 \times 203.2$ mm^3 in the streamwise, x, wall-normal, y, and spanwise, z, directions, respectively. The corresponding instantaneous velocity components are denoted as u, v and w, respectively. Upstream of the channel, a settling chamber containing honeycombs and screens followed by a nozzle with area ratio of $4:1$ is used for controlling/reducing the inflow turbulence level. Pressure taps on both sides of the nozzle are also used for monitoring the mean speed. On the downstream side, a mild diffuser with expansion angle of less than $7°$ links the channel with the main loop. The channel has four removable windows spanning its entire width, two on the top and two on the bottom, for installing walls with different shapes, roughness, and material properties. In the present investigation, the compliant wall is installed in the bottom downstream window, while the other three windows are mounted with rigid acrylic plates.

The wall consists of a homogeneous layer of transparent polydimethylsiloxane (PDMS) with thickness of $l_0 = 16$ mm attached to a 9 mm thick acrylic wall. This silicon rubber layer is 1250 mm long in the x-direction, and it spans the entire width of the channel (203.2 mm). The leading edge of this layer is located 1900 mm ($75h$) downstream of the channel entrance, where h ($= 25.4$ mm) is the channel half-height. The detailed procedures for moulding this compliant layer directly on the acrylic base in a special vacuum chamber with polished flat acrylic walls are described in Zhang *et al.* (2015). The mechanical properties of the PDMS have been measured by a Rheometrics Solids Analyzer (RSA II) using another moulded sample of the same
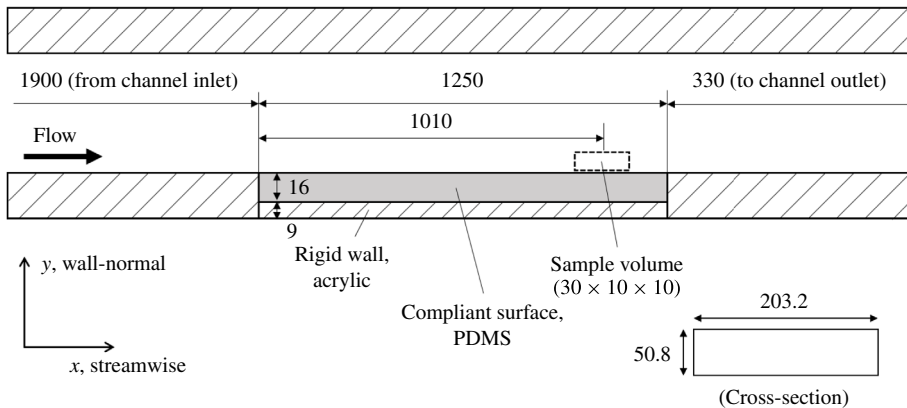
FIGURE 1. Schematic of the test section and location of the sample volume (drawn not to scale). All dimensions are in mm.

material, curing temperature and base-to-curing agent ratio. The frequency-averaged (0.1–12 Hz) storage modulus, E', is 0.93 MPa and the loss modulus, E'', is 0.07 MPa. The density of the PDMS, ρ_c, is 1.03×10^3 kg m^{-3}. The Poisson's ratio, σ, has not been measured, but based on Mark (1999), it is expected to be 0.5. The resulting shear modulus, estimated using $G = E'/2(1 + \sigma)$ is 0.31 MPa, and the shear wave speed calculated from $c_t = (G/\rho_c)^{1/2}$ is 17 m s^{-1}. The magnitude of c_t is significantly higher than the channel centreline velocity during the present experiments (2.5 m s^{-1}), implying that this material falls in the 'stiff wall' category. Hence, large-amplitude static-divergence waves are not expected to develop.

The working fluid in the channel is an aqueous solution of sodium iodide (NaI, 62 % by weight). The fluid density, ρ, and kinematic viscosity, ν, are 1.8×10^3 kg m^{-3} and 1.1×10^{-6} m^2 s^{-1}, respectively, and its refractive index, n_{NaI}, is 1.493. This refractive index is very close to that of the acrylic, which minimize light reflection at the rigid channel wall. However, it is also different from that of the compliant material ($n_{PDMS} = 1.413$), which is crucial for measuring surface deformation using interferometry. In the present experiments, the channel centreline velocity, U_0, is 2.5 m s^{-1}, and the friction velocity, u_τ, determined from a linear fit of the total shear stress profile, is 0.102 m s^{-1} (Zhang *et al.* 2015). The resulting viscous length scale, $\delta_\nu = \nu/u_\tau$, is 11 µm, and the corresponding time scale, $\tau_\nu = \nu/u_\tau^2$, is 105.7 µs. The friction Reynolds number, Re_τ, is 2300. Following the usual convention, a superscript $+$ is used to denote quantities normalized by u_τ and τ_ν.

2.2. *Velocity and pressure measurements*

The experimental set-up for the integrated time-resolved TPIV and MZI measurements is illustrated in figure 2. Detailed descriptions of this system and data analysis procedures, especially those involving MZI, are provided in Zhang *et al.* (2015). This section describes the main components briefly. Background on TPIV can be found in, for example, Elsinga *et al.* (2006) and Scarano (2013), and applications in boundary layers and channel flows are discussed in, for example, Schröder *et al.* (2008, 2011), Atkinson *et al.* (2011) and Schäfer *et al.* (2011). The present $30 \times 10 \times 10$ mm^3 ($2778 \times 926 \times 929\delta_\nu^3$) sample volume in the x, y and z directions, respectively, is located 1010 mm (39.8h) downstream of the leading edge of the compliant wall and
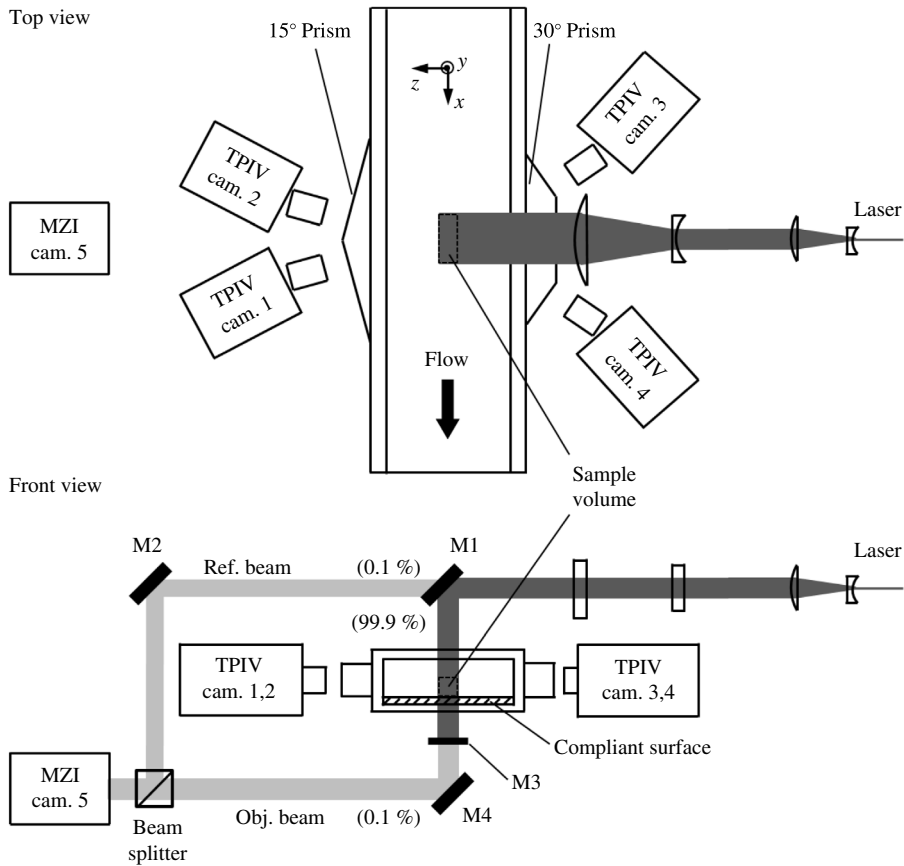
FIGURE 2. Optical set-up for the combined tomographic PIV and MZI system. Reprinted with permission from Springer.

2910 mm (114.6*h*) from the entrance of the channel. These length scales allow the flow to develop to nearly a fully developed state before reaching the sample volume, consistent with criteria provided by Antonia & Luxton (1971), and in agreement with measurements performed in the same channel over a rough wall by Hong *et al.* (2011). However, the channel is not sufficiently long to reach a 'fully developed' state based on the mean velocity measurements of Monty (2005). Furthermore, as discussed in Dean (1978), Monty (2005) and Hong *et al.* (2011), the 4 : 1 aspect ratio of the cross-section is not sufficient for establishing a 2D channel flow free of side effects. The flow field is illuminated at 6 kHz using a Photonics model DM60-527 Nd:YLF laser. The beam is expanded into a thick slab, and mirror M1 with back-polished surface, which serves as a beam splitter, directs 99.9 % of the light to the sample volume. Mirror M3 located under the channel reflects the majority of the laser energy back to the sample volume to increase the illumination intensity. The 6 kHz images are recorded at a resolution of 1200×600 pixel by four high-speed cameras (pco.dimax) located on both sides of the channel at the same elevation as the sample volume. Recording images through an air–acrylic interface at large angle of incidence causes undesired optical distortions, such as astigmatism. The astigmatism is minimized when the lens axis is perpendicular to the interface, achieved by attaching

acrylic prisms to the channel wall. The cameras are inclined relative to the lenses by the Scheimpflug angles to maintain all the sample volume in focus.

The flow is seeded with silver-coated hollow glass spheres. The mean particle diameter, d_p, is 13 µm ($d_p^+ = 1.2$), and its density, ρ_p, is 1.6×10^3 kg m^{-3}. The corresponding particle relaxation time $\tau_s = d_p^2 \rho_p / (18 \rho \nu)$ is 7.6 µs, and the Stokes number, τ_s / τ_ν, is 7.2×10^{-2}. Thus, except for elevations that are comparable to or smaller than d_p, where the scale of characteristic flow features is of the same order as the particle diameter, the particles are expected to follow the turbulent channel flow. The two-step calibration procedure has been performed before reconstructing 3D particle positions. Following procedures described in Scarano (2013), in the first step, a 2D target plate made from perforated metal sheet is placed inside the channel and translated in the z-direction over the entire width of the sample volume (10 mm). Images of this target plate are used to generate a 'coarse' mapping function, for projecting the coordinates in the 3D space to the 2D camera planes. In the second step, this mapping function is refined by volume self-calibration (Wieneke 2008) using actual particle images. The resulting disparity maps show 0.1 voxel uncertainty in locating the particle positions (Zhang *et al.* 2015). Subsequently, the instantaneous particle intensity distributions in 3D space are reconstructed using the simultaneous multiplicative algebraic reconstruction technique (SMART, Atkinson & Soria 2009) for the first five iterations, and then the CSMART algorithms (private communication with LaVision) for the last two iterations. The reconstructed volume consists of $1380 \times 638 \times 611$ voxels, in which a single voxel has a size of 18.8 µm ($1.7\delta_\nu$). The particle displacements are calculated using multi-pass direct volumetric cross-correlations between two successive frames. The size of the interrogation volume in the final pass is 48^3 voxels (0.905^3 mm^3, $82.3\delta_\nu$). Using a 75 % overlap between adjacent windows, we obtain $115 \times 53 \times 51$ vectors per realization with a vector spacing of $l = 0.226$ mm ($l^+ = 20.6$). This TPIV data analysis procedure is performed using LaVision DaVis 8.1 software package. In later discussions, the vorticity components, as well as the velocity gradient tensor are calculated from the velocity field using second-order central differencing. To identify vortices, the distributions of λ_2 are also computed, which is the intermediate eigenvalue of $\mathbf{S}^2 + \mathbf{\Omega}^2$, where $\mathbf{S}$ and $\mathbf{\Omega}$ are the symmetric and anti-symmetric parts of the velocity gradient tensor (Jeong & Hussain 1995).

The uncertainty of TPIV has been studied in several previous publications using different methods. For example, Elsinga *et al.* (2006) generate synthetic particle images using the flow field of a vortex ring. They demonstrate displacement uncertainty of 0.1 and 0.16 voxel for the in-plane and out-of-plane components, respectively. Worth, Nickels & Swaminathan (2010) generate synthetic particle images using DNS data of isotropic turbulence. Their mean displacement uncertainty is 0.2 and 0.3 voxel for the in-plane and out-of-plane components, respectively. Atkinson *et al.* (2011) compare TPIV and hot-wire anemometry in a turbulent boundary layer. A large bias error ($\sim$1.5 voxel) occurs in the near-wall region ($y^+ = 15$), where the velocity gradients are high. Their overall displacement uncertainty is approximately $\varepsilon_u \Delta t = 0.6$ voxels, where ε_u is the velocity uncertainty, and Δt the time delay between exposures. Following Moffat (1988), ε_u is estimated from the r.m.s. values of the fluctuating velocity divergence, $\langle (\partial u_i' / \partial x_i)^2 \rangle^{1/2} = (3/2)^{1/2} \varepsilon_u / l$, where l is the vector spacing, $\langle \, \rangle$ represents an ensemble average, $'$ indicates fluctuating quantiles and repeating indices indicates summation. The same approach is utilized in the present study, resulting in a 0.3 voxel displacement uncertainty, corresponding to a velocity uncertainty of 0.036 m s^{-1}, or 1.4 % of U_0. The uncertainty in ensemble-averaged

velocity, estimated by dividing ε_u by the square root of the number of measurements, is two orders of magnitude smaller.

A brief summary of the GPU-based procedures for using the time-resolved 3D velocity field to calculate the pressure distribution is provided in appendix B. The material acceleration is calculated utilizing a Lagrangian method proposed by Liu & Katz (2006), and expanded in Liu & Katz (2013). However, unlike the previous work that is based on planar measurements, the present analysis is based on 3D data. The instantaneous pressure distribution is subsequently calculated by spatially integrating the material acceleration. The viscous term is neglected since the ratio between the viscous term and material acceleration is of the order of 10^{-5} based on the present TPIV data, in agreement with observations by van Oudheusden *et al.* (2007) and Ghaemi *et al.* (2012), the latter for boundary layers. The integration is performed by extending the virtual-boundary omni-directional integration method (Liu & Katz 2013) to three dimensions. This pressure calculation algorithm is validated using DNS results for a channel flow available in the Johns Hopkins Turbulence Databases (Perlman, Burns & Li 2007; Li *et al.* 2008; Graham *et al.* 2016) by comparing the reconstructed 3D pressure with the known values available from the simulation. The r.m.s. value of the relative integration error (only) is 0.46 %, a negligible effect in comparison to that caused by errors in material acceleration. Similar to procedures used for estimating ε_u, the uncertainty in material acceleration is estimated from the r.m.s. value of its curl, $\nabla \times (\mathrm{D}u_i'/\mathrm{D}t)$. Provided that the viscous terms in the Navier–Stokes equation can be neglected, $\nabla \times (\mathrm{D}u_i'/\mathrm{D}t)$ should be equal to zero. Assuming isotropy, $\varepsilon(\mathrm{D}u_i'/\mathrm{D}t)/l \approx \langle (\nabla \times (\mathrm{D}u_i'/\mathrm{D}t))^2 \rangle^{1/2}$, where ε represents the uncertainty. Using the present data, the estimated uncertainty in material acceleration is 32 m s^{-2}, which is approximately 45 % of the spatially averaged r.m.s. value of $\mathrm{D}u_i'/\mathrm{D}t$. Since the pressure is integrated from its gradient and averaged over multiple integration directions, the relationship between $\varepsilon(p)$ and $\varepsilon(\nabla p)$ can be estimated as $\varepsilon(p) \approx \varepsilon(\nabla p)Nl/(NM)^{1/2} \approx \rho Nl/(NM)^{1/2}\varepsilon(\mathrm{D}u_i'/\mathrm{D}t)$, where N is the number of grid points along one integration path and M is the number of integration paths. The values of N and M depend on the location of the sample point, but vary by 10 % across the sample volume. Using the current parallel line omni-directional integration procedure, the spatially averaged values for N and M are 33 and 10 242, respectively. Substituting these values in the equation for $\varepsilon(p)$, the corresponding uncertainty in instantaneous pressure is 0.7 Pa, which is less than 2 % of the spatially averaged r.m.s. value of pressure fluctuations. This analysis does not fully account for the effect of limited spatial resolution very near the wall.

Since the pressure is integrated from its gradient, an undetermined reference pressure is needed as an integration constant. Following Joshi *et al.* (2014), we use the spatially averaged pressure over the entire sample volume, p_{ref} (t), for each instantaneous realization. Hence, the pressure field discussed in the rest of the paper, p (x, y, z, t), represents the deviation of the pressure at a specific point from the spatially averaged value. Due to the finite size of the sample volume, p (x, y, z, t) effectively represents a spatially high-pass filtered pressure, and the resulting spectra do not account for the time dependence of the spatially averaged pressure. Similar issues are also encountered when solving the pressure Poisson equation to determine the pressure, which requires a Dirichlet-type boundary condition for some of the boundaries. Several recent studies have used the Bernoulli equation for a boundary located away from the wall (e.g. de Kat & van Oudheusden 2012; Ghaemi & Scarano 2013). For application in boundary layer flow, Ghaemi *et al.* (2012) examine the effect of the elevation of the Dirichlet boundary, showing that the calculated wall pressure does not differ substantially when this boundary is located above 0.2*h*.

2.3. *Surface deformation measurements*

The 2D surface deformation is measured using Mach–Zehnder interferometry (MZI, Hecht 2002). The optical components are integrated into the TPIV system, as illustrated in the front view of figure 2. Mirrors M1 and M3, which are located on top and under the channel, respectively, and are polished on both sides, allow transmission of 0.1 % of the laser energy through them. The light transmitted through M1 serves as reference beam, and the light passing through the channel and M3 is the object beam. As the latter propagating through the transparent compliant surface, the surface deformation alters the optical path length of the light, affecting its phase distribution. The fringe patterns generated as the two beams interfere are recorded by a fifth high-speed camera (pco.dimax) at 3000 f.p.s. using 1584×1024 pixel arrays. The fringe spacing, S, is approximately 34 pixels (374 µm or $34\delta_v$). A total of 7838 frames have been recorded, corresponding to a duration of 2.6 s ($2.5 \times 10^4 \tau_v$). For the combined system, the field of view (FOV) is 17.4×11.3 mm^2 ($1611 \times 1046\delta_v^2$) in the x and z directions, respectively. The size of this sample area is matched with the corresponding dimensions of the TPIV volume. A sample original fringe pattern is provided in figure 3(*a*,*b*), with the latter zooming on a small area indicated in figure 3(*a*) by a dashed rectangular box. In a separate series of experiments, which involve only deformation measurements and are aimed at observing larger scale wall surface features, the FOV of MZI system is expanded to 90×54 mm^2 ($8182 \times 4909\delta_v^2$), resulting in a 25 times increase in sample area. The optical set-up is illustrated in figure 4. Here, the object beam is expanded and collimated by a pair of concave (L1) and convex (L2) lenses, and then propagates through the channel. The corresponding image size is increased to 2016×1200 pixels and the sampling rate reduces to 2000 f.p.s. The fringe spacing is approximately 11 pixels (498 µm or $45\delta_v$). Total of 5255 frames have been recorded, corresponding to a duration of 2.6 s ($2.5 \times 10^4 \tau_v$).

Details about the data processing procedures, including validations using synthetic images, are provided in Zhang *et al.* (2015), and only summarized briefly in this paper. The surface shape is calculated from the phase distribution of the object wave. The three analysis steps include: (i) fringe enhancement, (ii) phase evaluation, and (iii) phase unwrapping. The intensity distribution of the interferogram can be expressed as

$$I(x, z, t) = C_1(x, z, t) + C_2(x, z, t) \cos[\varphi_0(x, z) + \delta(x, z, t)], \qquad (2.1)$$

where C_1 is the sum of the intensities of the object and reference waves, and C_2 is twice the product of the amplitudes of the two waves. The phase of fringes contains two terms. The first, φ_0, is presumed to be stationary and accounts for the shape of the wavefront, including effects of window shapes, unperturbed compliant surface thickness, distortion by lenses, etc. The second term, δ, is the time-dependent phase difference between the two waves resulting from changes to the thickness of the wall, $d(x, z, t)$. It satisfies

$$\delta(x, z, t) = \frac{2\pi}{\Lambda} (n_{PDMS} - n_{Nal}) \, d(x, z, t), \qquad (2.2)$$

where Λ is the laser wavelength, 527 nm in the present measurements. As is evident from figure 3(*a*), the original interferograms are quite noisy due to laser non-uniformity and distortions. Hence, a series of enhancement procedures have been developed and implemented to homogenize the fringe amplitude by filtering out spatial features that are larger or smaller than the fringe spacing. This process results
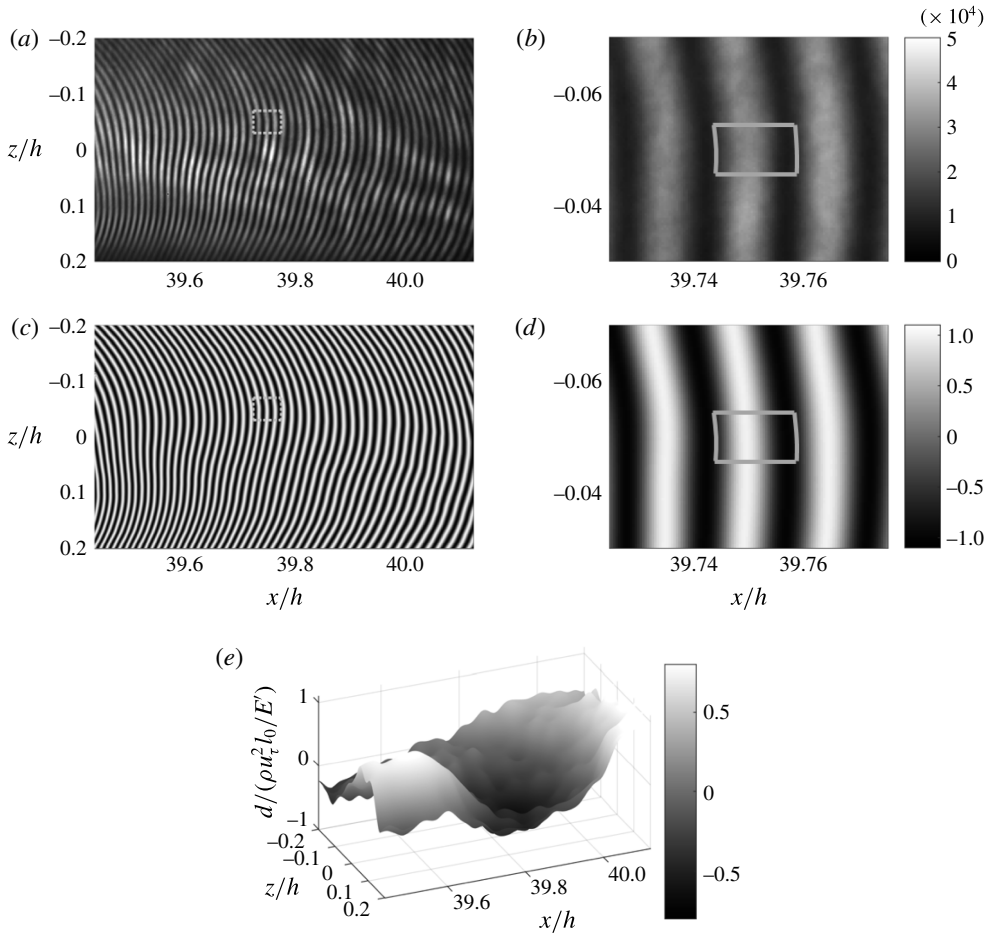
FIGURE 3. (*a,b*) Sample instantaneous image of raw MZI fringe pattern, (*c,d*) the same image after correlation-based enhancement, and (*e*) the corresponding linearly detrended distribution of deformation, with vertical scales exaggerated. (*a,c*) Entire field of view. (*b,d*) Zooms on the small area indicated by dashed lines. The enclosed area in the zoomed views shows a correlation mask.

in $C_1 = 0$ and $C_2 = 1$. The enhancement procedure involves two steps. In the first, the instantaneous intensity in every pixel is normalized based on the maximum and minimum intensities for that pixel over a time interval of length $\Delta T = 312\tau_\nu$. This choice for ΔT is long enough to obtain converged image statistics, but short enough to account for temporal variations in, for example, laser intensity. In the second enhancement step, the iso-phase intensities are homogenized and bandpass filtered by calculating the spatial autocorrelation of the image in a small interrogation window centred at the pixel of interest. The resulting autocorrelation map is considered as a template of the local fringe pattern, which preserves the fringe shape, but loses the phase information since the autocorrelation always peaks at the centre. The lost phase is recovered by cross-correlating the autocorrelation with the original image, which provides the local filtered intensity. The choice of window size for calculating the (auto- and cross-) correlations has a strong impact on the enhancement error.
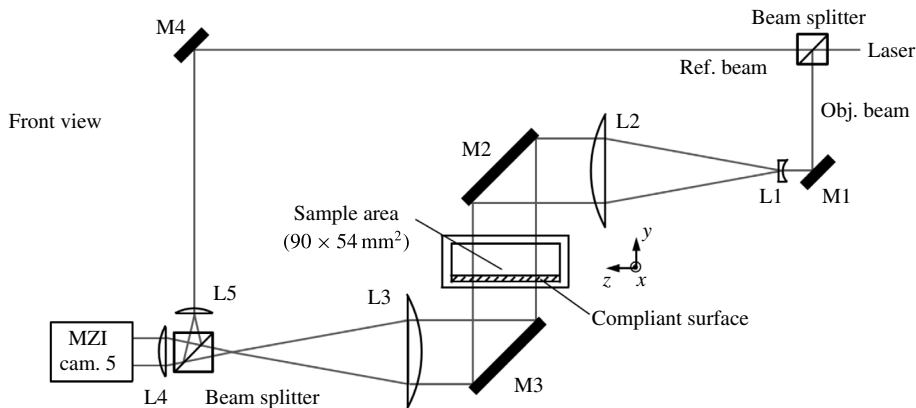
FIGURE 4. Optical set-up for the extended field-of-view MZI system.

To minimize the error, the analysis described in Zhang *et al.* (2015) shows that in a direction perpendicular to the iso-phase lines, the window width should span an integer multiple of the local fringe spacing. This requirement is achieved by utilizing a mask, which is indicated in figure 3(*b*,*d*). The shapes of the left and right boundaries follow the local fringe iso-phase lines, and their distances are equal to one fringe cycle. Calibrations using synthetic data also show that the window height should be smaller than $(SR)^{1/2}$, where R is the local radius of curvature of the fringes. For the present fringe spacing, this requirement is achieved by reducing the height of the window to 20 pixels. To reduce the processing time, instead of performing this analysis for every pixel, the cross-correlation values from one calculation is used to update a 5×5 pixels region located in the centre of the interrogation window. Uncertainty analysis indicates that the impact of repeating the correlations for every 25 pixels is negligible. The enhanced interferogram is shown in figure 3(*c*,*d*). Evidently, the background intensity variations are removed, and the fringe intensities are normalized to the range $[-1, 1]$.

Several techniques are available to extract phase distributions from interferograms. A widely adopted approach is the so-called 'Fourier transform' method (Ichioka & Inuiya 1972; Takeda, Ina & Kobayashi 1982). Although easy to implement, this method is prone to errors near the edge of the interferogram due to spectral leakage. Improved methods aimed at addressing this problem (e.g. Bone, Bachor & Sandeman 1986; Roddier & Roddier 1987) are typically based on extending the image beyond its original boundary by various extrapolation methods. They reduce the errors near boundaries, but do not eliminate them completely. Consequently, we opt to use a different approach which does not involve a Fourier transform. Taking advantage of the uniform fringe intensity provided by the correlation-based filtering, the phase distribution can be directly evaluated using an arccosine function. The phase ambiguity introduced by arccosine can be readily removed if the sign of the actual phase slope along a certain direction is known by, for example, imposing a slope that is larger than that at any point in the sample area. In the present setting it is simply achieved by tilting the reference beam relative to the object beam by a 'large' angle ($\sim 0.08°$). This is the reason that the fringes in figure 3 are aligned approximately in the spanwise direction. They are also slightly curved, mostly due to the optical distortion associated with the channel walls.

The corrected phases are still 'wrapped', with values varying between 0 and 2π, and need to be unwrapped temporally and spatially. Temporal unwrapping is performed on the intensity time series of a fixed pixel located at the centre of the image using a 1D unwrapping algorithm (Itoh 1982). It identifies and removes 2π phase discontinuities along this time series. The resulting phase at this location is used as the starting value for the spatial unwrapping of each interferogram. The spatial 2D phase unwrapping is achieved by spatially integrating the phase gradient. This integration should be path-independent if the wrapped phase map is free from residues. These residues can be identified by performing the closed-loop integral/summation of the wrapped phase gradient for every 2×2 pixels over the entire image (Ghiglia, Mastin & Romero 1987; Goldstein, Zebker & Werner 1988). For the combined TPIV/MZI data, the phase map has very small (negligible) residues. Hence, a straightforward integration is performed to unwrap the phase, first along columns and then across rows. In the large FOV MZI experiments, the extended FOV reveals local imperfections on the compliant surface not visible in the previous test. They appear in a few spots as tightly packed and sometimes discontinuous fringes. Hence, the Goldstein's algorithm (Goldstein *et al.* 1988; Ghiglia & Pritt 1998) is utilized to filter the impact of these points out for the large FOV dataset. This algorithm first connects nearby residues of different signs with straight lines, and then generates integration paths that do not cross those lines.

Time-averaging of the unwrapped phase distributions is used to determine the stationary term $\varphi_0(x, z)$ in (2.1). Its distribution is subtracted from the instantaneous data, leaving only $\delta(x, z, t)$. The surface deformation is then calculated using (2.2). Figure 3(*e*) shows the instantaneous deformation calculated from the interferogram presented in figure 3(*c*) and normalized with $\rho u_\tau^2 l_0/E'$. The deformation is spatially linearly detrended to remove displacements larger than the current FOV, and highlight the local spatial variations. Extensive synthetic validations have been performed using fringes generated from known deformation fields (Zhang *et al.* 2015). The effect of background noise has been accounted for by adding a noisy background extracted from experimental data. The results indicate the fringe spacing, its radius of curvature, as well as its spatial gradient, $|\partial S/\partial x|$, have the strongest impacts on the errors. Specifically, the error increases for decreasing $|SR|$ and increasing $|\partial S/\partial x|$. For fringes similar to the present experimental data, the r.m.s. value of the measurement uncertainty determined from these validations is ~ 0.01 μm (Zhang *et al.* 2015). As discussed later, although the amplitude of the total deformations (~ 100 μm) is much larger than the current uncertainty, the amplitude of the high-pass filtered deformations which are advected with the flow, is approximately 0.1 μm, only one order of magnitude larger than the estimated uncertainty.

A sample instantaneous realization of the combined TPIV/MZI data is shown in figure 5. The bottom wavy contour surface shows the deformation of the compliant wall high-pass filtered at $\omega h/U_0 = 4.3$, where ω is the frequency in radians per second. As discussed later, this cutoff frequency enables us to focus on advected phenomena. The amplitude of the surface motion is exaggerated for clarity. The 3D vectors in the *x*–*y* plane represent the velocity fluctuations, and only alternate vectors are shown in the streamwise direction. The colour contours indicate distribution of wall-normal velocity. The 3D blob represents iso-surfaces of $\lambda_2/(U_0/h)^2 = -6.2$, which indicate the location of vortex structures (Jeong & Hussain 1995). In this sample, the deformation peak and trough appear to be associated with the wall-normal velocity and predominantly strong vortices. Classification of these structures is the primary objective of this paper. A sample instantaneous realization of the large FOV high-pass
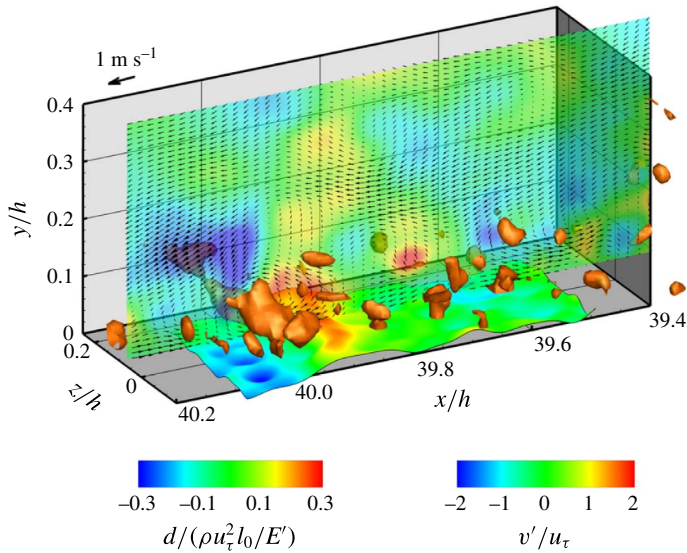
FIGURE 5. A sample instantaneous realization of the flow field and detrended and high-pass filtered surface deformation. Colour contour in the x–y plane shows the distribution of v'. The 3D blobs are iso-surfaces of $\lambda_2/(U_0/h)^2 = -6.2$. For clarity only alternate vectors are shown in the streamwise direction.
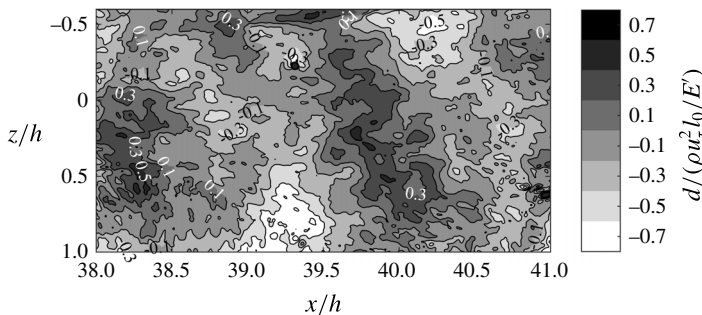

FIGURE 6. A sample instantaneous realization of the large field-of-view detrended and high-pass filtered (at $\omega h/U_0 = 1.6$) deformation.

filtered (at $\omega h/U_0 = 1.6$) deformation is shown in figure 6. Here, the deformation pattern appears to be largely aligned in the spanwise direction, with a streamwise wavelength of approximately $1.9h$. The movies indicate that this pattern is advected at approximately the centreline velocity (see supplementary movie 1 available on https://doi.org/10.1017/jfm.2017.299). A small circular region located at ($x/h = 39.3$, $z/h = -0.2$) contains a local surface defect on the compliant wall.

3. Results

3.1. *Mean velocity and Reynolds stresses profiles*

Profiles of the mean velocity and Reynolds stresses are presented in figure 7. The statistics are calculated from 17 689 velocity fields acquired over a duration of 2.95 s ($2.8 \times 10^4 \tau_v$). The spatially averaged integral time scale $\tau = \int R_{u,u} \, \mathrm{d}s$, where $R_{u,u}(s)$ is
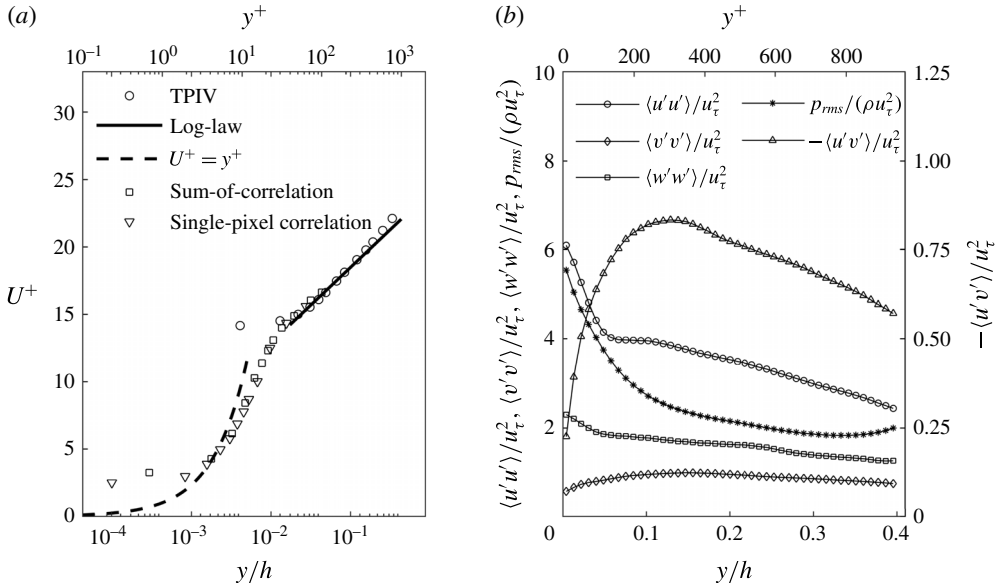
FIGURE 7. (*a*) The mean velocity profile measured using 'standard' TPIV, sum-of-correlation and single-pixel ensemble correlation. The results are compared with the log-law profile: $U^+ = (1/\kappa) \ln y^+ + B$, ($\kappa = 0.41$; $B = 5.2$) and $U^+ = y^+$. (*b*) Profiles of Reynolds stresses calculated using the 'standard' TPIV data, and r.m.s. values of pressure fluctuations calculated using omni-directional integration.

the autocorrelation function of the streamwise velocity, is 0.0115 s. As a result, data acquisition time corresponds to 257τ. The spatially averaged mean velocity profile (figure 7*a*) is compared with the log-law profile: $U^+ = (1/\kappa) \ln y^+ + B$, where $\kappa = 0.41$ and $B = 5.2$, as well as with $U^+ = y^+$ in the viscous sublayer (Pope 2000). The wall-normal distance is normalized using h, indicated in the bottom axis, and using δ_ν shown in the top axis. This velocity profile calculated from the 'standard' TPIV shows a clear log-law region, but it is erroneous, as expected, in the buffer layer, where a vector spacing of $l^+ = 20.6$ is too coarse. Two related techniques are utilized to extract the near-wall velocity. The first one is the sum-of-correlation method (Meinhart, Wereley & Santiago 2000), which determines the mean velocity at each location from an ensemble-averaged correlation map for small interrogation windows. To enhance the particle image concentrations, in the present calculation, the 3D particle distributions are projected onto 2D images by assigning the maximum intensity along the spanwise direction to each pixel. The ensemble-averaged distribution of correlations is calculated for an 8×8 pixels interrogation window with 75 % overlap. An alternative approach is the 'single-pixel ensemble correlation' (Westerweel, Geelhoed & Lindken 2004; Scharnowski, Hain & Kahler 2012; Soria & Willert 2012), which is equivalent to reducing the interrogation window down to one pixel. These calculations are also performed using the above-mentioned 2D projected images. Results of both techniques are also included in figure 7(*a*). Evidently, they extend the velocity profile down to the buffer layer, but deviate from the expected linear velocity profile for $y^+ < \sim 2$. This deviation is not surprising considering that the particle diameter is approximately $1.2\delta_\nu$.

The Reynolds stresses profiles, $\langle u'u' \rangle / u_\tau^2$, $\langle v'v' \rangle / u_\tau^2$, $\langle w'w' \rangle / u_\tau^2$, $-\langle u'v' \rangle / u_\tau^2$, and $p_{rms} / \rho u_\tau^2$ are presented in figure 7(*b*). The distribution of $\langle u'u' \rangle / u_\tau^2$ peaks near the wall,

considering that the buffer layer is not resolved, followed by a plateau extending to $y/h \sim 0.1(y^+ \sim 230)$. Both have been observed before in experiments and simulations (e.g. Hutchins & Marusic 2007*a*; Mathis, Hutchins & Marusic 2009; Hultmark, Bailey & Smits 2010; Marusic, Mathis & Hutchins 2010; Mathis, Hutchins & Marusic 2011; Hultmark 2012; Schultz & Flack 2013; Bernardini, Pirozzoli & Orlandi 2014; Lee & Moser 2015). The height of the plateau is also consistent with those of Schultz & Flack (2013) for similar Re_τ. By inspecting the energy spectra of the streamwise velocity at various elevations, Hutchins & Marusic (2007*a*) associate the plateau with energy contributed by large-scale log-layer motions. They also demonstrate that these large-scale structures modulate the amplitude of the near-wall streamwise velocity fluctuations, a phenomenon relevant to the present investigation. The Reynolds shear stress $-\langle u'v' \rangle/u_\tau$ peaks around $y/h \sim 0.12(y^+ \sim 280)$. As shown in Zhang *et al.* (2015), we estimate the wall stress by extrapolating the total shear stress, namely the sum of the viscous and Reynolds stresses, to the wall. The result is used for normalizing all the present ensemble-averaged variables, and agrees with the mean velocity profile (figure 7*a*). The elevation of the Reynolds stress peak is slightly higher than those found in Hoyas & Jiménez (2006) and Schultz & Flack (2013) at similar Reynolds numbers ($Re_\tau = 2000$). It is presumably associated with the size of the TPIV interrogation volume of $82.3\delta_\nu$, which attenuates the small-scale fluctuations near the wall (Hong *et al.* 2011; Talapatra & Katz 2013). The values of $p_{rms}/\rho u_\tau^2$ decrease with elevation, consistent with those reported in Tsuji *et al.* (2007) and Joshi *et al.* (2014) for boundary layers at similar Reynolds numbers. DNS results for channel flow at $Re_\tau = 1020$ by Abe, Matsuo & Kawamura (2005) show a similar trend with elevation, but their magnitudes are lower by approximately 50 %. An increase in pressure fluctuations with increasing Reynolds number has been observed experimentally (Tsuji *et al.* 2007) and in simulated data (Lozano-Durán & Jiménez 2014).

3.2. *Spectra of pressure and deformation*

The spatial power spectral density (PSD) of pressure, $E_{pp}(k_x)$, normalized by $\tau_w^2 \nu/u_\tau$, at two elevations are presented in figure 8. Here, $k_x = 2\pi/\lambda_x$ is the streamwise wavenumber. For the current analysis, we opt to present directly measured spatial spectra because, as noted before, by setting the spatially averaged instantaneous pressure to zero, the pressure signal is spatially high-pass filtered. Hence, it is also expected to attenuate a not readily determined part of the frequency spectrum. The spectra are calculated using FFT without windowing using all the instantaneous realizations over the entire spanwise range, and then spatially and ensemble-averaged. The results are normalized with inner scaling and compared with the measured PSD of pressure calculated from planar PIV data (Joshi *et al.* 2014) in the same facility, but for a developing boundary layer. The axes normalized with outer scaling are added for comparison, based on the present experimental conditions. The present results are also compared to the PSD of DNS-based wall pressure data of Abe *et al.* (2005) for channel flow. At low wavenumbers, the present results agree with those of Joshi *et al.* (2014) for the same elevation. However, they deviate at high wavenumbers, with the present values being lower, presumably owing to differences in the dimensionless spatial resolution. In Joshi *et al.* (2014), the interrogation window size is $35.8\delta_\nu$ versus $82.3\delta_\nu$ for the present data. Furthermore, the 75 % overlap utilized in the TPIV analysis also causes aliasing at high wavenumbers (Foucaut, Carlier & Stanislas 2004; Schrijer & Scarano 2008). The present PSD is higher
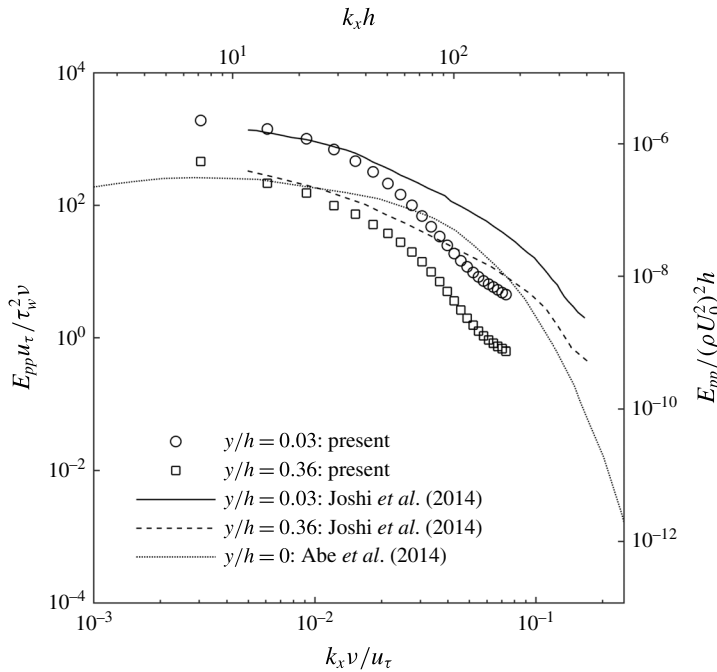
FIGURE 8. The present power spectral density of pressure compared with previous experimental and DNS results.

than that of Abe *et al.* (2005), presumably due to differences in Reynolds number, consistent with trends shown by them.

The PSD of the deformation, $E_{dd}(\omega)$, normalized by $h(\rho u_\tau^2 l_0 / E')^2 / U_0$, calculated from the small FOV data is shown in figure 9(*a*). The spectrum is calculated for each surface node for the entire duration of the measurement, and then spatially averaged. As is evident, the surface motions involve a broad range of time scales, with an r.m.s. value of 42 μm. Part of the motions are associated with channel vibrations, whose length scales are presumably much larger than the FOV. Hence, they displace or tilt the entire FOV. Bi-directional linear detrending of instantaneous realization filters these motions out, as done for the rest of this paper. The PSD of the detrended deformation is shown in figure 9(*b*). The corresponding r.m.s. value is 0.2 μm ($0.02\delta_\nu$). Hence, the present detrended deformations are not expected to have a significant impact on the flow structure in the boundary layer, resulting in a 'one-way coupling', where the flow affects the wall, but not vice versa. After detrending, the spectrum has two troughs, at $\omega h / U_0 \sim 1.6$ and ~ 4.3. i.e. it can be roughly divided into three frequency bands: (i) $f < 25$ Hz or $\omega h / U_0 < 1.6$, (ii) 25 Hz $< f < 67$ Hz and (iii) $f > 67$ Hz or $\omega h / U_0 > 4.3$, as indicated by two vertical lines. A visual inspection of the temporally filtered deformation for each of these bands (see supplementary movies 2–4) indicates that only deformations in the highest frequency band are dominated by downstream-travelling surface patterns. The dominant motions in the first and second bands seem to propagate in all directions, and sometimes behave like standing waves. It should be noted that these waves have much lower amplitude and they occur at much lower velocity (relative to the c_t) than the static-divergence wave reported in Hansen & Hunston (1974, 1983) and Gad-el-Hak *et al.* (1984). The PSD
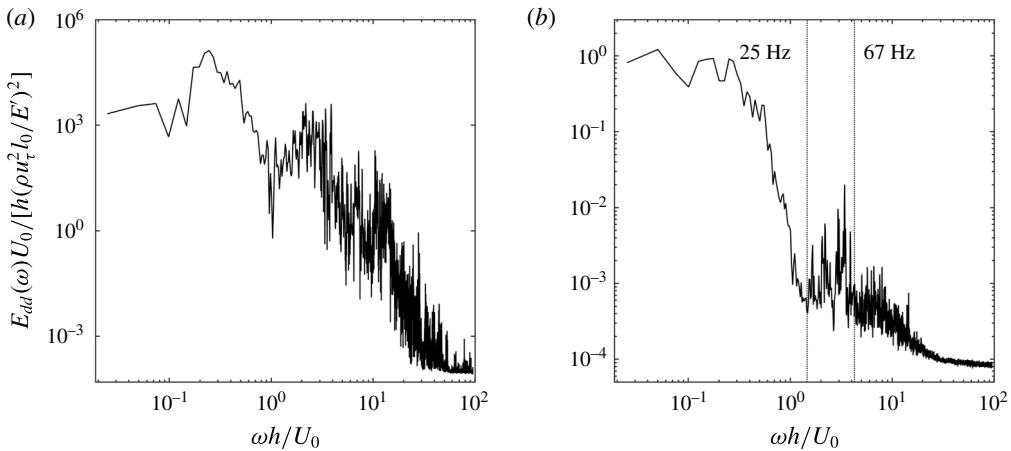
FIGURE 9. Power spectral density of the normalized deformation (*a*) before spatial detrending and (*b*) after spatial detrending. Reprinted with permission from Springer.

of the detrended deformation for the large FOV is presented in figure 10. The corresponding r.m.s. value is 0.18 μm, still much smaller than the wall unit, and are not expected to have a significant effect on the flow structure. The location of trough at $\omega h/U_0 \approx 1.6\text{--}1.8$ is consistent with that shown in figure 9(*b*), but $\omega h/U_0 = 1.8$ also corresponds to a deformation with wavelength equal to the length of the sample area (90 mm) travelling at a velocity of 2.5 m s^{-1}, the centreline velocity. The peaks at $\omega h/U_0 < 1.8$ correspond to non-advected phenomena, and do not have a consistent direction of propagation. In subsequent analysis, most of our attention focuses on the advected phenomena. The large FOV spectrum does not have a trough at $\omega h/U_0 \sim 4.3$, confirming that the dip in figure 9(*b*) is caused by detrending.

To elucidate the shape of the spectrum for $\omega h/U_0 > 1.8$, one can analyse the response of a compliant layer to pressure perturbations. Chase (1991) introduces a classical model for the response of a viscoelastic layer under prescribed pressure and wall shear stress fluctuations. Because of its significance to the present study, the model is summarized in appendix A. Briefly, this 2D model involves streamwise and wall-normal small-amplitude deformations in a domain with thickness of l_0 unbounded in the *x*-direction. Using Helmholtz decomposition, the displacement and stresses of the compliant layer are solved for a viscoelastic material. The material damping is accounted for by allowing complex longitudinal and shear wave speeds in the Navier equation. The prescribed pressure, shear as well as fluid loading serve as boundary conditions. As shown in appendix A, for the present range of frequencies, wavenumbers, material properties, and magnitude of pressure fluctuations relative to those of shear stresses (Tsuji *et al.* 2007, 2012), the impact of pressure on the shape of the wall is higher by orders of magnitudes than that of shear stresses. Hence, the present analysis focuses on the effect of pressure. Figure 11 shows the normalized wavenumber–frequency spectrum of wall deformation predicted by the Chase (1991) model for sinusoidal pressure excitation with equal amplitude ($= \rho u_\tau^2$) at all wavenumbers and frequencies. Both the frequency and wavenumber are normalized using two different variables, with those involving l_0 and c_t being associated with the model directly, and those involving h and U_0 being added in order to relate the results to the flow conditions. The peak response occurs at $k_x l_0 \approx 2\pi/3$. At higher
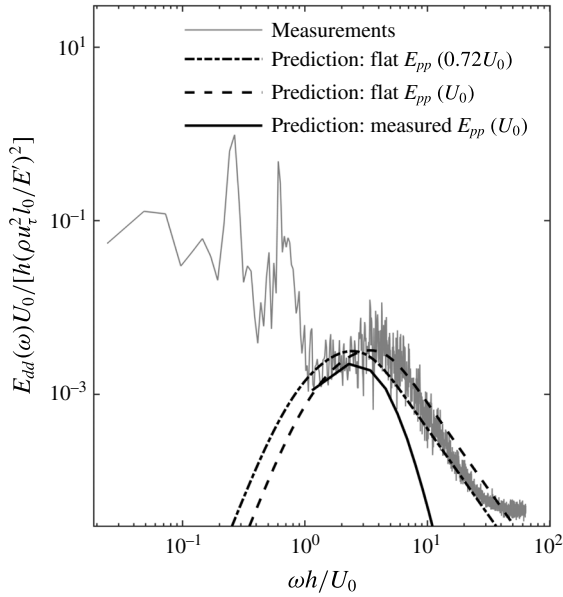
FIGURE 10. Power spectral density of the large field-of-view detrended deformation. The lines show predictions of the Chase (1991) model for flat pressure spectra with phase speeds of $0.72U_0$ (dash-dot line) and U_0 (dashed line), as well as the measured pressure spectra at $y/h = 0.03$ for a phase speed of $0.72U_0$ (thick line).
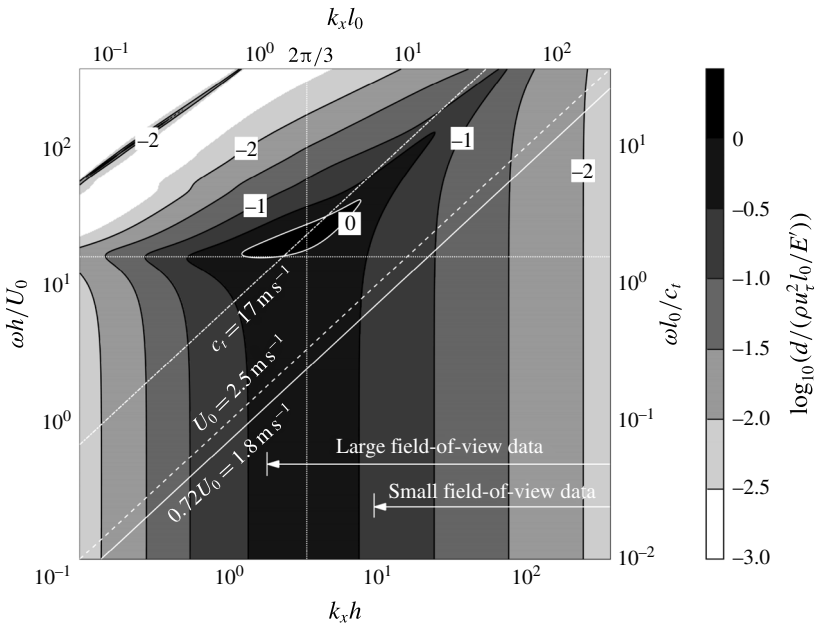

FIGURE 11. The amplitude of deformation (normalized by $\rho u_\tau^2 l_0/E'$) in response to pressure perturbation amplitude of ρu_τ^2, as predicted by the Chase (1991) model. The inclined lines correspond to the specified advection speeds. The vertical and horizontal dotted lines represent $k_x l_0 = 2\pi/3$ and $\omega l_0/c_t = 1.45$, respectively.

wavenumbers, i.e. to the right of the vertical dotted line, the surface response peaks when the pressure phase speed is slightly lower than c_t. The latter is highlighted by the inclined dash-dot line. Evidently, since the present centreline velocity, which is indicated by a dash line, is much lower than c_t, the interactions between the compliant wall and the flow are substantially weaker than the peak values.

For $\omega l_0/c_t < 1.45$, the surface response over the entire domain has a broad peak centred at $k_x l_0 \approx 2\pi/3$. For the current study, the peak wavelength, $3l_0$, is equal to $1.89h$. Hence, this wavelength is covered by the large FOV, but not by the small FOV, as highlighted in figure 11. Consequently, the deformation features dominating the large FOV data (figure 6) have a wavelength of $\sim 1.9h$, which cannot be observed in the small FOV. The vertically aligned spectral peak at low frequencies ($\omega l_0/c_t < 1.45$) indicates that the wavenumber corresponding to the spectral peak is only a function of l_0, and does not depend on the phase speed of the pressure perturbation. Consequently, within this spectral domain, one can readily tailor the surface response to flow excitation by varying the compliant layer thickness. This statement is relevant to cases involving stiff compliant material, where the shear speed is significantly higher than the flow speed. At low wavenumbers ($k_x l_0 < 2\pi/3$), the surface response is high at a frequency of $\omega l_0/c_t \approx 1.45$, i.e. slightly below $\pi/2$, as indicated by a horizontal dotted line. This frequency corresponds to two roundtrips across the compliant layer at a phase speed of c_t. For the present experimental conditions, advected phenomena in the relevant frequency range have a very short wavelength. Hence, the present conditions do not fall in the relevant frequency–wavenumber bandwidth to excite these modes.

For flow features propagating at the centreline velocity or similar values (U_0 and $0.72U_0$ are shown in figure 11), the intersection of the phase speed with the wavenumber–frequency spectrum provides a prediction for the frequency spectrum. This prediction assumes that the amplitude of pressure perturbations does not vary with frequency. The resulting spectra are presented as the flat E_{pp} lines in figure 10 for pressure excitation with advection speeds of $0.72U_0$ and U_0, and amplitude of $1.3\rho u_\tau^2$. This amplitude is selected to match that of the measured E_{dd}. As is evident, the shapes of the predicted and measured deformation spectra appear to agree for frequencies falling in the $1 < \omega h/U_0 < 12$ range. The frequency of the peak response at $\omega h/U_0 \approx 4$, is better predicted when U_0 is used as the advection speed. The analysis can be repeated for frequency- (or wavenumber-)dependent pressure amplitude using the measured pressure spectrum (figure 8). The result, which is also presented in figure 10 and labelled as 'measured E_{pp}' is based on the pressure spectrum, including amplitude, at $y/h = 0.03$ ($y^+ = 70$). This spectrum has a similar shape as the others, but values are lower, and the peak location agrees with that corresponding to an advection speed of $0.72U_0$. It appears that the Chase (1991) model predicts the response of the present 'stiff' compliant wall to advected pressure excitation. Conversely, below $\omega h/U_0 \approx 1$, the model and measured spectra diverge, presumably, since this range is dominated by features that are not advected with the flow, as the deformation movies show (supplementary movie 2). They might be associated with, for example, resonances or reflected waves associated with the finite boundaries of the compliant wall.

The measured streamwise wavenumber–frequency spectra of detrended deformation, $E_{dd}(k_x, \omega)$, normalized by $[h(\rho u_\tau^2 l_0/E')]^2/U_0$ for the small and large FOV are presented in figure 12(a,b), respectively. They are calculated separately for each spanwise location using FFT in the streamwise and time directions. The resulting spectra are then spanwise-averaged. The small FOV data, which is presented on linear scales,
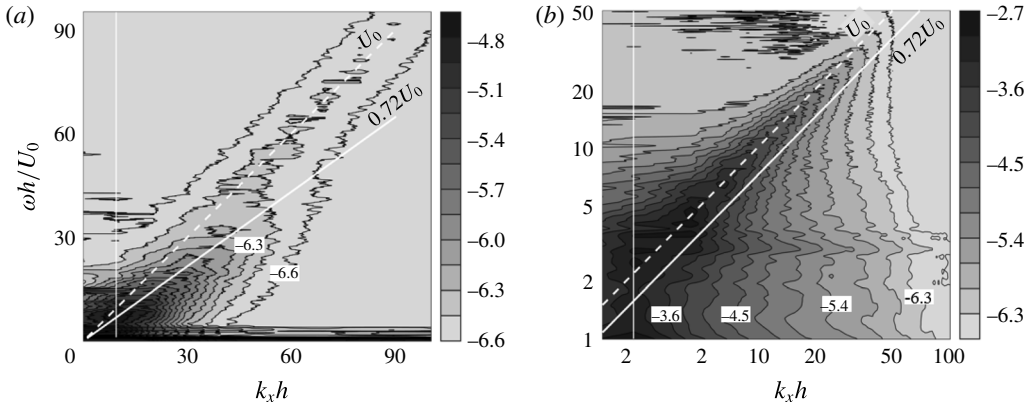
FIGURE 12. The measured wavenumber–frequency spectra of detrended deformation, with contours indicating the values of $\log_{10}\{E_{dd}(k_x, \omega)U_0/[h(\rho u_\tau^2 l_0/E')]^2\}$. (*a*) Small field-of-view data on linear axes, with an incremental increase between contour lines of 0.15. (*b*) Large field-of-view data on logarithmic axes, with an incremental increase between contour lines of 0.3. The inclined solid and dashed lines represent advection speeds of $0.72U_0$ and U_0, respectively. The vertical lines in each figure show the wavenumber of the corresponding field of view.

has two inclined bands representing two advection modes of different speeds, which are presumably associated with flow structures located at different elevations in the boundary layer. In subsequent discussions, we refer to them as a 'slow mode', with an advection speed of $0.72U_0$, and a 'fast mode' with speed of U_0. The choices of pressure advection speeds in figure 11 are based on these modes. The fast mode band extends to higher frequencies and wavenumbers than the slow mode. The simulation of Kim & Choi (2014) also show a preferred advection speed of $0.72U_0$, for stiff compliant surfaces, consistent with the present slow mode, but do not show a fast mode. At low frequencies, i.e., $\omega h/U_0 < 4.3$, the spectral contours are largely aligned in the horizontal direction, indicating that this range is dominated by non-advected features with nearly zero phase speed. Such bands have also been observed in the DNS results of Kim & Choi (2014), which they attribute to resonances of the spring and damper system that they utilize to model the compliant wall.

The k_x-ω spectrum for the large FOV (figure 12*b*) is presented in logarithmic scale to highlight the low-frequency/wavenumber range. Here, at low wavenumber/frequency, the advection band is dominated by the fast mode, which is marked by a white dashed line. At high frequencies, the peak appears to tilt towards lower phase speeds, which falls between the fast and slow modes, the latter being marked by a solid white line. The differences between figure 12(*a*,*b*) for overlapping wavenumber ranges, in particular the lack of a distinct slow mode in the latter, can be attributed to the scale of the low-pass filtering and detrending. For a given frequency, large scales are attenuated more than small ones with decreasing filter size. Consequently, the fast mode is attenuated more than the slow mode in the detrended small FOV data, making the latter more visible. This effect has been verified by detrending the large FOV data at the small FOV scales. Results (not shown) confirm that the slow mode becomes more noticeable. Figure 12(*b*) also shows that energy corresponding to the fast mode extends to scales that are larger than the small FOV ($k_x h < 9.4$), consistent with the visual observations of large-scale deformation features moving at
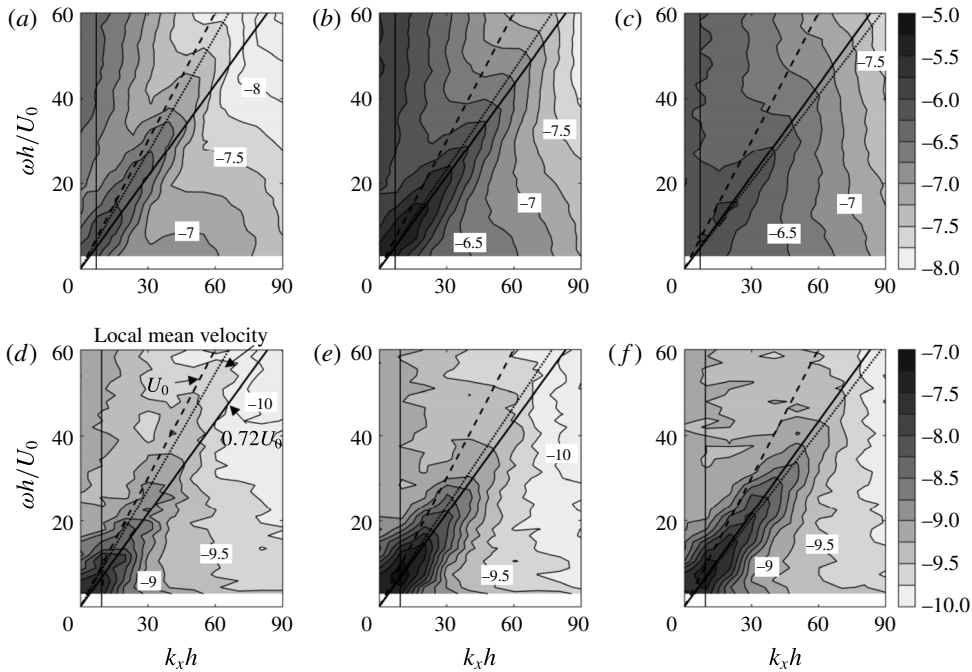
FIGURE 13. (*a–c*) Wavenumber–frequency spectra of pressure at (*a*) $y/h = 0.35$, (*b*) $y/h = 0.12$ and (*c*) $y/h = 0.05$. (*d–f*) Pressure–deformation wavenumber–frequency cross-spectra at (*d*) $y/h = 0.35$, (*e*) $y/h = 0.12$ and (*f*) $y/h = 0.05$. The dashed lines, solid lines and dotted lines correspond to phase speeds of U_0, $0.72U_0$ and the local mean velocity, respectively. The vertical lines in each figure show the wavenumber of the corresponding field of view. The grey scales on (*a–c*) and (*d–f*) indicate the values of $\log_{10}\{E_{pp}(k_x, \omega)U_0/[h(\rho u_\tau^2)]^2\}$ and $\log_{10}\{E_{pd}(k_x, \omega)U_0/[h^2(\rho u_\tau^2)(\rho u_\tau^2 l_0/E')]\}$, respectively.

the centreline velocity (e.g. figure 6). With increasing FOV, the measurements should cover advected features that have frequencies falling below $\omega h/U_0 \sim 4.3$. Indeed, figure 12(*b*) shows that part of the energy at $\omega h/U_0 < 4.3$ corresponds to advected modes at low wavenumbers, where the spectral peak is located, but a substantial fraction is not. These features cannot be seen in the detrended small FOV surface shape, leaving only non-advected features at frequencies falling below $\omega h/U_0 \sim 4.3$ (67 Hz), and creating the spectral dip at this frequency in figure 9(*b*).

In subsequent discussions, we correlate the flow structure and pressure field to the surface deformation. Considering that for the small FOV experiment, which provides the relevant data, frequencies corresponding to $\omega h/U_0 < 4.3$ do not contain advected modes. In the analysis that follows, the pressure and deformation are high-pass filtered at $\omega h/U_0 = 4.3$. Intuitively, correlating the flow with the surface shape has to start with the pressure field. Hence, the pressure $k_x - \omega$ spectra, $E_{pp}(k_x, \omega)$ at three elevations, namely $y/h = 0.35$, 0.12 and 0.05, are presented in figure 13(*a–c*), respectively. They are calculated separately for each spanwise location, and then spatially averaged. The corresponding pressure–deformation cross $k_x - \omega$ spectra, $E_{pd}(k_x, \omega)$, aimed at identifying pressure modes that affect the deformation, are presented in figure 13(*d–f*). They show the amplitude of the Fourier transform of the cross-correlation between deformation and pressure at the specified elevation. Each plot shows the centreline velocity (or the fast mode) as a dashed line, the slow mode, $0.72U_0$, as a solid line,

and the local mean velocity as a dotted line. All the pressure spectra show elevated energy at low wavenumber over a broad frequency range. This artefact is a direct result of setting the spatially averaged pressure over the entire sample volume to zero in the present analysis. In reality, this unavailable reference pressure varies in time, and zeroing it introduces a low wavenumber jitter. To partially resolve this problem, Ghaemi & Scarano (2013) use the Bernoulli equation to obtain a boundary condition away from the wall. Using this approach to estimate the reference pressure (e.g. on the upper surface) or frequency low-pass filtering of the signal decreases the magnitude of this band (not shown). This band has no significant effect on the present analysis, and we opt not to manipulate the signals further. At all elevations, the pressure spectra contain clear advection bands at speeds that decrease with elevation, and do not differ substantially from the corresponding mean velocity. This advection band is not as distinct at the lowest elevation (figure 13c), but is still evident. The pressure–deformation cross-spectra in figures 13(d–f) also show clear advection bands at all elevations, with a phase speed that decreases with elevation. For the pressure at $y/h = 0.12$ and 0.05, the phase speeds do not differ significantly from the slow mode or the local mean velocity. As for the pressure at $y/h = 0.35$, the advection band is largely concentrated in the low-frequency/wavenumber range, and the advection speed appears to span between the slow mode and the local mean velocity. With increasing frequency, the band tilts more towards the local mean velocity. A comparison between figures 13(a) and 13(d) suggests that the compliant wall is preferentially affected by the large-scale pressure features. With decreasing distance from the wall, the range of scales affecting the wall deformation expands. Assuming that the strength of eddies increases with their size, but their influences decrease with distance from their centre (the latter being clearly true for vortices), the expanding influence band with decreasing distance from the wall should be expected. These findings are consistent with findings of previous wall pressure fluctuations claiming that the observed scale dependence of the advection speeds is associated with the location of eddies in the boundary layer, with the smaller ones being preferentially located closer to the wall (e.g. Willmarth & Wooldridge 1962; Bull 1967; Blake 1970; Wills 1970; Dinkelacker *et al.* 1977; Choi & Moin 1990; Jeon *et al.* 1999; Ghaemi & Scarano 2013; Salze *et al.* 2015).

3.3. *Conditional correlations between deformation and flow variables*

This section examines the relations between deformation and flow structure based on spatial correlations between the surface shape and flow variables (pressure, velocity, vorticity, etc.), as well as between pressure and other flow variables. The spatial conditional correlation between two functions, $f(x, y, z, t)$ and $g(x, y, z, t)$, is defined as

$$R_{f,g}(\Delta x, \Delta y, \Delta z)|_{f>\sigma_f}$$
$$= \frac{\langle f(x_0, y_0, z_0, t)g(x_0 + \Delta x, y_0 + \Delta y, z_0 + \Delta z, t)\rangle|f(x_0, y_0, z_0, t) > \sigma_f}{\sigma_f(x_0, y_0, z_0)\sigma_g(x_0 + \Delta x, y_0 + \Delta y, z_0 + \Delta z)} \quad (3.1)$$

the parameters involved are specified in the subscript, σ_f and σ_g are the r.m.s. values of f and g. In all cases, the correlations are calculated based on fluctuating components of each variable, but there is no need to subtract mean values for pressure and deformation because both are high-pass filtered. To highlight phenomena, in many of the correlations, we impose a condition of, for example, a deformation larger or
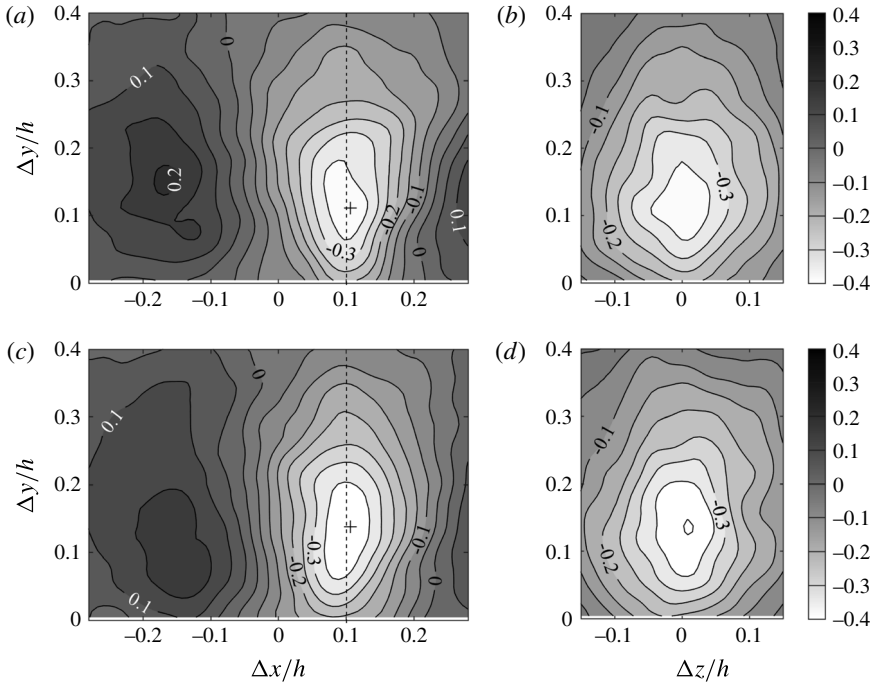
FIGURE 14. Conditional correlations between the detrended and high-pass filtered (at $\omega h/U_0 = 4.3$) deformation at $(0, 0)$ and pressure, based on (a,b) strong positive deformation $(d > \sigma_d)$ and (c,d) strong negative deformation $(d < -\sigma_d)$. The y–z planes in (b,d) correspond to $\Delta x/h = 0.1$, which is marked by dashed lines in (a,c). The position of peak value is indicated by a $+$.

smaller than its r.m.s. value, i.e. $d(x_0, y_0, z_0) > \sigma_d$ or $d(x_0, y_0, z_0) < -\sigma_d$, respectively. The condition is indicated in the definition of the variable. In such cases, the r.m.s. values of f and g are still calculated from the original un-conditioned data. In correlations that do not involve any conditions, $R_{f,g}$ is used instead.

Distributions of deformation–pressure conditional correlations based on large positive $(d > \sigma_d)$ event, $R_{d,p}|_{d>\sigma d}$, for the $(\Delta x, \Delta y, \Delta z = 0)$ and $(\Delta x = 0.1h, \Delta y, \Delta z)$ planes are presented in figure 14(a,b), respectively. Results conditioned on $d < -\sigma_d$ events, $R_{d,p}|_{d<-\sigma d}$, are shown in figure 14(c,d), respectively. In all cases, the correlations are calculated for all surface points and then spatially averaged. As is evident, for positive deformation (bump), the negative correlation peak is located at $\Delta x/h \approx 0.1$ and $\Delta y/h \approx 0.12$, i.e. the deformation lags behind the negative pressure influencing it most by $\sim 0.1h$ in the streamwise direction. A second positive correlation peak with lower magnitude is located upstream, representing a high-pressure region. The streamwise separation between the positive and negative correlation peaks is approximately $0.25h$, suggesting that the length scale of the pressure field relevant to the deformation is approximately $0.5h$. The mean velocity at $\Delta y/h = 0.12$, $0.77U_0$, is close to that of the deformation phase speed of the slow mode, $0.72U_0$. It appears that structures affecting the wall deformation are located in the log-layer, at nearly the same elevation of the Reynolds shear stress peak (figure 7b), and slightly above the plateau in streamwise velocity fluctuations. The resolution of present velocity and pressure measurements is too coarse for probing the buffer layer. However, the
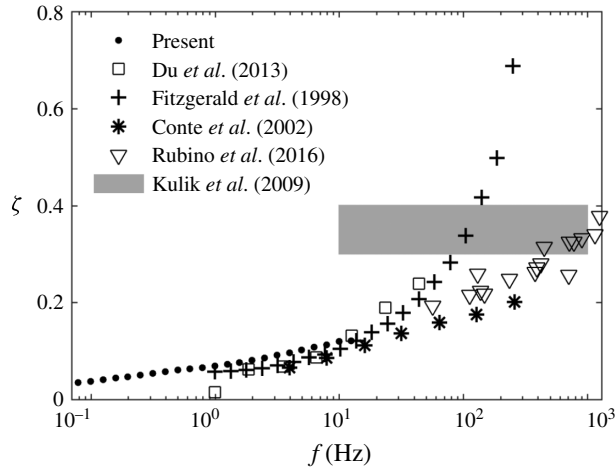
FIGURE 15. The loss tangent of PDMS based on the current measurement and several other sources.

resolution of deformation measurements is sufficient for identifying structures as small as $0.015h$. Yet, the wavenumber–frequency spectra of deformations (figure 12*a*) indicate that they are dominated by phenomena having characteristic length scale larger than $0.13h(290\delta_v)$. Eddies with such scales are likely to reside in the log and/or outer layer, and are less likely to be located in the buffer layer. The *y–z* distribution of correlation in figure 14(*b*) is presented in a plane ($\Delta x = 0.1h$) that coincides with the streamwise peak in figure 14(*a*). The *y–z* correlation peak is located at the same elevation as that in the perpendicular plane and centred around $\Delta z = 0$. The distributions corresponding to negative deformation (figure 14*c,d*) appear to be quite similar to those associated with positive deformation, with the same streamwise offsets. However, since $d < -\sigma_d$, a negative correlation indicates positive pressure. Furthermore, the elevation of the correlation peak is slightly higher, which is located at $\Delta y/h \approx 0.14$.

The next discussion is aimed at explaining the streamwise offset between pressure and deformation. It involves both the effect of damping by the compliant wall, as well as the structure of the pressure field in the boundary layer. Starting with the damping effect, one can use the Chase (1991) model to estimate phase lag. It requires knowledge of the viscoelastic properties of the compliant material, which are characterized by using complex moduli, i.e., $E' + iE''$, (e.g. Fung 1965; Ferry 1970), with E' being the storage modulus, and E'' the loss modulus. The key parameter is the frequency-dependent loss tangent, $\zeta = E''/E'$. As shown in figure 15, the loss tangent of the PDMS utilized in the present study has only been measured in a low-frequency range (0.1–12 Hz), using the only instrument available to us. Data from several other sources (Fitzgerald & Fitzgerald 1998; Conte & Jardret 2002; Kulik *et al.* 2009; Du *et al.* 2013; Rubino & Loppolo 2016) are compiled in the same plot in order to extend the frequency to conditions that are relevant for the present study. The shaded area in figure 15 covers the range of results of a series of measurements performed by Kulik *et al.* (2009) for samples of various sizes. It appears that various results collapse below 10 Hz, but are scattered over a broad range above 67 Hz. To estimate the damping-induced phase lag, we start with $\zeta = 0.3$, but repeat the calculation for other values as well. The streamwise offset between wall pressure and
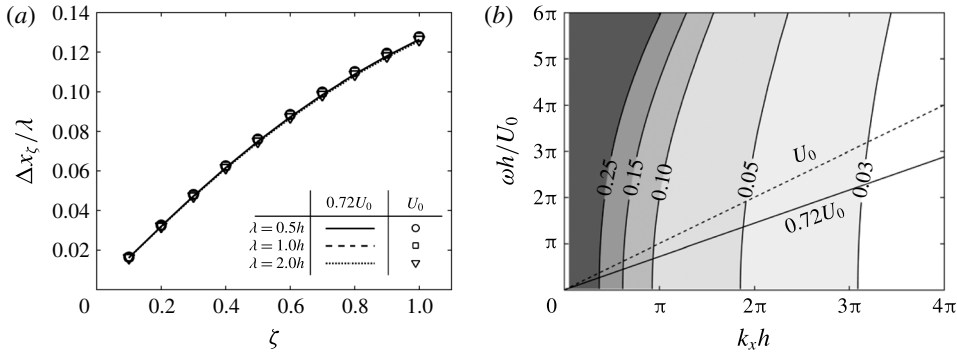
FIGURE 16. The streamwise offset between deformation and pressure correlation peak predicted by the Chase (1991) model: (*a*) values of $\Delta x_\zeta / \lambda$ for pressure perturbations with the specified wavelengths and advection speeds, and (*b*) values of $\Delta x_\zeta / h$ as functions of wavenumber and frequency for $\zeta = 0.3$.

surface deformation based on the Chase (1991) model, Δx_ζ, is shown in figure 16. Figure 16(*a*) demonstrates the effect of ζ for pressure waves with wavelengths of $\lambda / h = 0.5$, 1.0 and 2.0*h* and advection speeds of $0.72U_0$ (lines) and U_0 (symbols). As is evident, the values $\Delta x_\zeta / \lambda$ nearly collapse for the relevant range of phase speeds, i.e. $\Delta x_\zeta / \lambda$ is only weakly dependent on the frequency. The magnitude of $\Delta x_\zeta / \lambda$ increases with increasing ζ, an expected trend because the associated increase in relaxation time (Ferry 1970). The weak effect of frequency is demonstrated in figure 16(*b*), which shows the distribution of $\Delta x_\zeta / h$ for a fixed loss tangent of 0.3. Clearly, the contour lines are nearly vertical for the relevant range, indicating that varying the phase speed while keeping the wavelength constant has little effect on Δx_ζ. Based on figure 14, choosing $\lambda = 0.5h$, the model predicts a spatial offset of $0.024h$, roughly 24 % of the observed value. Using higher (but reasonable) values for ζ, for example, $\zeta = 0.4$, would increase Δx_ζ to $0.03h$, i.e. it still explains only a fraction of the measured offset. The rest must be related to the structure of the pressure field in the boundary layer.

The structure of the pressure field in the channel flow can be inferred from two-point correlation of pressure, $R_{p,p}$, which is plotted in figure 17 for a reference point located at $y_0 / h = 0.12$. Consistent with many previous results (e.g. Kim 1989; Tsuji *et al.* 2007; Ghaemi & Scarano 2013; Joshi *et al.* 2014), the correlation contours are inclined at a rather large angle relative to the mean flow. Using the locus of points along which the correlation value has the slowest decay (white line), the estimated inclination angle around $y_0 / h = 0.12$ is 68°. A linear extrapolation of this line to $y = 0$ suggests that the wall pressure lags by $0.048h$ behind the field pressure at $y_0 / h = 0.12$. A more accurate approach involves calculation of the distribution of pressure phase in the wavenumber–frequency cross-spectra of pressure at two different elevations,

$$
\begin{aligned}
C_{p,p}(k_x, \omega; y) = {} & \left[\int p(x, y, z_0, t) e^{-ik_x x} e^{-i\omega t} \, dx \, dt \right]^* \\
& \times \left[\int p(x, y_0 = 0.12h, z_0, t) e^{-ik_x x} e^{-i\omega t} \, dx \, dt \right].
\end{aligned} \tag{3.2}
$$

Here, $*$ denotes complex conjugate. The magnitude of the complex $C_{p,p}$ quantifies the level of correlation between the two signals. Its argument is the phase difference,
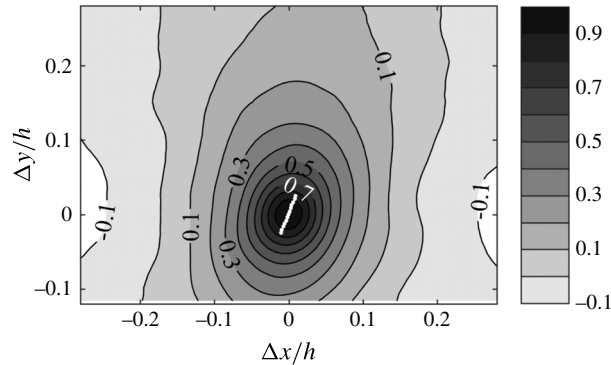
FIGURE 17. Distribution of two-point correlation of pressure ($R_{p,p}$) for a reference point located at $(0, 0.12h, 0)$.

$\Delta \Phi(y) = \Phi_{0.12_h} - \Phi$, between pressure at $y_0/h = 0.12$ and other elevations, as a function of k_x, ω and y. Taking into account the fact that different modes are not equally correlated, the characteristic streamwise offset is estimated from the $|C_{p,p}|$-weighted average of $\Delta\Phi/k_x$ over the entire spectrum. The procedure is performed separately for each spanwise location and then averaged. The resulting profile of $\Delta x_{p,p} = \Delta\Phi/k_x$ is presented in figure 18. Evidently, the wall pressure lags by $0.077h$ behind the pressure at $y/h = 0.12$. This value is higher than the result obtained from extrapolating the two-point correlations, because the magnitude of $R_{p,p}$ is dominated by local events, where the correlations are high. Hence, it is biased towards small-scale structures. Conversely, the spectral-based weighted-average value of $\Delta x_{p,p}$ favours highly correlated events across two elevations, namely large-scale structures as the distribution of $|C_{p,p}|$ demonstrates (not shown). This bias is consistent with the scales dominating the pressure–deformation cross-spectrum shown in figure 13(e), justifying the use of the spectral-based $\Delta x_{p,p}$ to estimate the streamwise offset. Figure 19 compares the measured streamwise offset (grey horizontal line) to the distribution of Δx_ζ (for $\zeta = 0.3$) and to the combined effect of material damping and structure of the pressure field, i.e. $\Delta x_\zeta + \Delta x_{p,p}$. The latter is provided for two values of ζ to show that its value does not have a significant effect on the conclusions. As is evident, the combined effect agrees with the observed lag for the relevant frequency range $4.3 < \omega h/U_0 < 40$, shown in figure 13(e). The phase lag between pressure and deformation appears to be caused in part ($\sim24\,\%$) by material damping, but for the most part by hydrodynamic phase lag between pressure in the log-layer, where the correlation peaks, and the wall pressure.

Correlations between surface deformation and flow velocity and/or vorticity distributions have been used in efforts aimed at identifying coherent flow structures associated with the wall shape. Here again, trends associated with large positive ($d > \sigma_d$) and large negative ($d < -\sigma_d$) deformations are displayed and discussed separately. The conditional correlations between wall deformation and three components of the velocity in selected planes are presented in figures 20 and 21. In these plots, the deformation is high-pass filtered at $\omega h/U_0 = 4.3$, but the velocity is not, to account for effects of structures larger than FOV (further discussion follows). The analysis is performed for all planes and then spatially averaged. In addition to correlations, figures 20 and 21 also show the conditionally averaged projection of streamlines onto the x–y and y–z planes, respectively, calculated from the
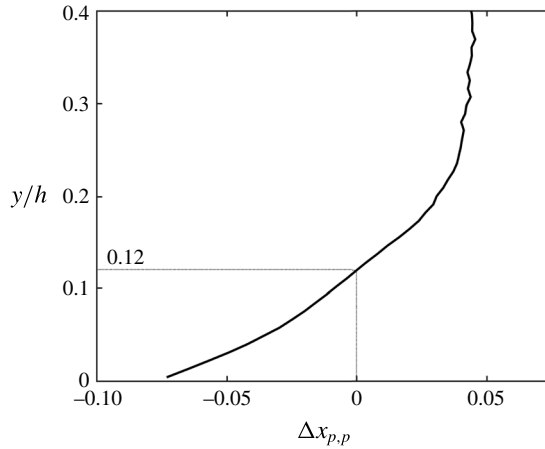
FIGURE 18. Profile of the average streamwise offset between the pressure at $y_0/h = 0.12$ and that at other elevations. The values are calculated from the amplitude-weighted argument of pressure–pressure cross-spectrum.
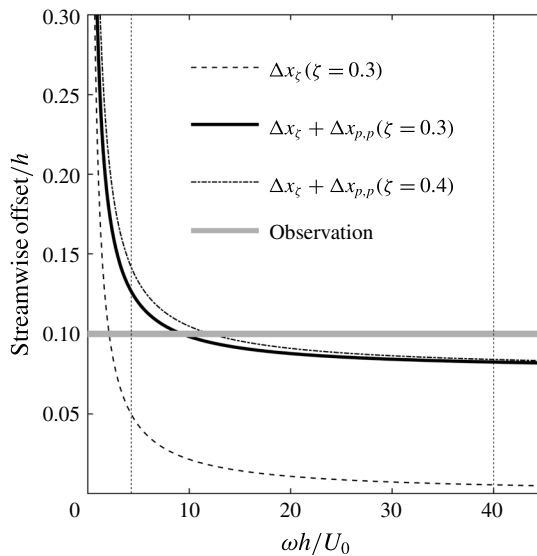

FIGURE 19. A comparison of the measured streamwise offset of the deformation–pressure correlation peak to that caused by damping only, and the combined effects of hydrodynamic phase lag and material damping. The latter is provided for two values of loss tangent.

corresponding velocity components. The y–z planes in figure 21 are presented at two streamwise locations, $\Delta x/h = 0$, where the deformation is measured, and $\Delta x/h = 0.1$, which is selected based on the peak of deformation–pressure correlations. In general, all the correlations associated with dimples are higher than those corresponding to bumps. Out of the velocity components, v' has the strongest correlation with the wall shape, followed by u' and w'. For positive deformations, the streamlines and signs of
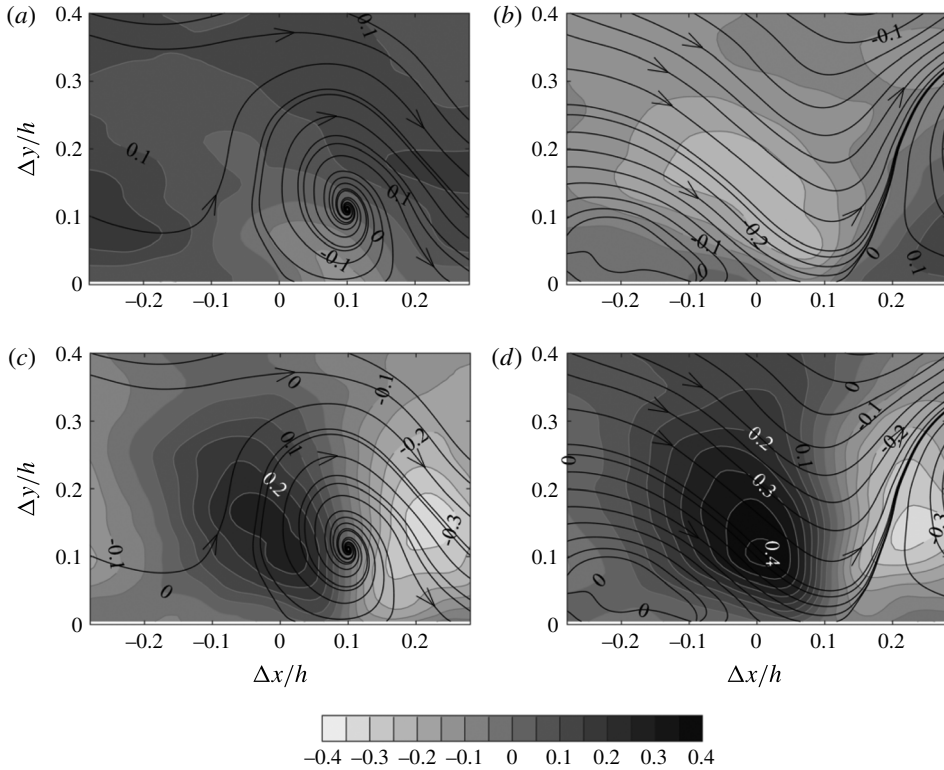
FIGURE 20. Conditional deformation–velocity correlations at $(\Delta x, \Delta y, \Delta z = 0)$ for positive (*a,c*) and negative (*b,d*) deformations: (*a*) $R_{d,u}|_{d>\sigma d}$, (*b*) $R_{d,u}|_{d<-\sigma d}$, (*c*) $R_{d,v}|_{d>\sigma d}$ and (*d*) $R_{d,v}|_{d<-\sigma d}$. The streamlines show the corresponding conditionally averaged flow fields.

correlations in figure 20(*a,c*) appear like a swirling flow with preferentially negative ω'_z centred at $\Delta x/h \approx 0.1$ and $\Delta y/h \approx 0.11$, very close to the peak of $R_{d,p}|_{d>\sigma d}$ in figure 14(*a*). Above the deformation, where the correlation values are high, there is a steep ejection-like flow (Q2, with $u' < 0$ and $v' > 0$). In the correlation maps involving spanwise velocity (figure 21*a,c*) the magnitudes are quite low. Based on the streamlines in figure 21(*a*), and the signs of $R_{d,v}|_{d>\sigma d}$ in figure 20(*c*), the flow direction above the deformation peak ($\Delta x/h = 0$) is consistent with 'anti-splatting', i.e. a flow converging from both spanwise directions and turning upward. Although the signs of $R_{d,w}|_{d>\sigma d}$ at $\Delta x/h = 0$ and $\Delta x/h = 0.1$ are similar, the vertical velocity at the latter is nearly zero.

For negative deformations, both the streamlines and distribution of correlation in figure 20(*b,d*) show a sweeping flow (Q4, with $u' > 0$ and $v' < 0$) above the deformation, and a transition between an upstream sweeping flow and a downstream ejection at $\Delta x/h \approx 0.1$. The zero-crossing of $R_{d,v}|_{d<-\sigma d}$ at $\Delta x/h \approx 0.1$ coincides with the streamwise plane of maximum deformation–pressure correlation. The y–z plane distribution of $R_{d,w}|_{d<-\sigma d}$ and streamlines at $\Delta x/h = 0$ (figure 21*b*) show a splatting flow impinging on the surface and turning outward in the spanwise direction. As shown in figure 22, the magnitude of the $R_{d,u}|_{d>\sigma d}$ and $R_{d,u}|_{d<-\sigma d}$ peaks increase significantly if the conditional correlations are calculated based on high-pass filtered velocity at $\omega h/U_0 = 4.3$, similar to what is done for the deformation. The same
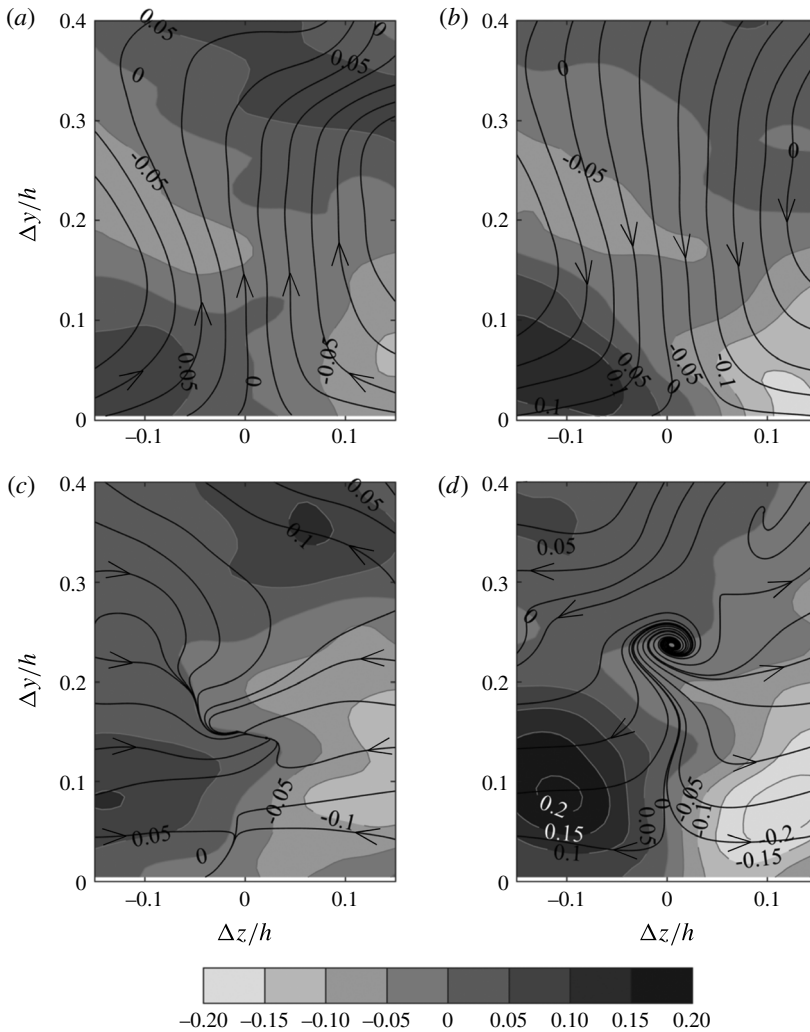
FIGURE 21. Conditional deformation–spanwise velocity correlations for positive ($R_{d,w}|_{d>\sigma d}$, a,c) and negative ($R_{d,w}|_{d<-\sigma d}$, b,d) deformations: (a,b) $\Delta x = 0$, bottom row; (c,d) $\Delta x = 0.1h$. The streamlines show the corresponding conditionally averaged flow fields.

increase occurs for correlations involving the other velocity components (not shown). For $d > \sigma_d$, the dominant phenomenon in the region of peak correlation and above the deformation is an ejection. For $d < -\sigma_d$, the flow direction reverses to a sweep over the same area. Apart from the higher correlation magnitudes, the only appreciable effect of filtering in the spatial distributions is a shift of $R_{d,u}|_{d>\sigma d}$ slightly upstream and away from the wall.

Given the connections established between deformation and pressure as well as between deformation and velocity, the 'loop' is closed by showing the distributions of conditional pressure–velocity (unfiltered) correlation in figure 23. They are based on the pressure measured at $y_0/h = 0.12$, where $\Delta x = \Delta y = 0$, and we follow the same procedures described for the deformation–velocity correlations, including spatial averaging over all planes, and calculation of the projection of conditionally
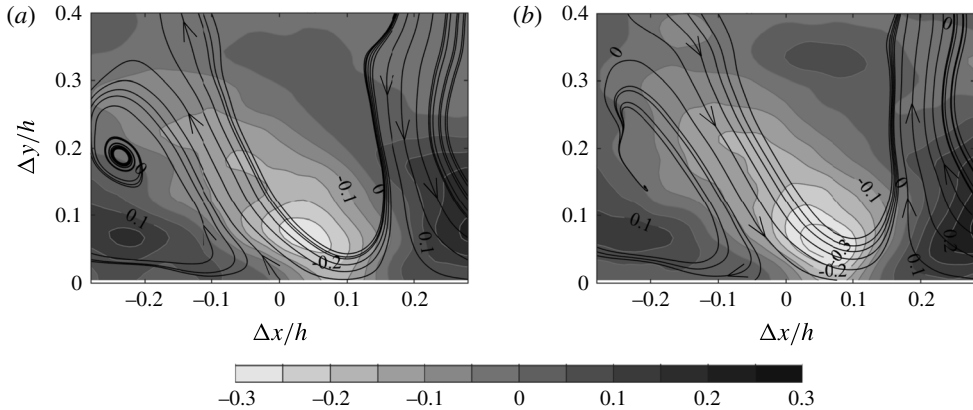
FIGURE 22. Distributions of conditional deformation–streamwise velocity correlations for high-pass filtered velocity at $\omega h/U_0 = 4.3$: (*a*) $R_{d,u}|_{d>\sigma d}$ and (*b*) $R_{d,u}|_{d<-\sigma d}$.

averaged streamlines. This elevation is selected in view of the deformation–pressure correlations. To facilitate comparisons with figure 20, panels (*a,c*) show results for $p < -\sigma_p$, and panels (*b,d*) correspond to $p > \sigma_p$. The wall-normal velocity component has the strongest correlation with pressure, in agreement with trends reported in Joshi *et al.* (2014), and consistent with trends of the deformation–velocity correlations. Although the shapes of streamlines differ, in part due to the elevation of the pressure conditioning point, the main flow feature in figure 23 for $p < -\sigma_p$ (distributions of $R_{p,u}|_{p<-\sigma p}$ and $R_{p,v}|_{p<-\sigma p}$ and corresponding streamlines) is a large-scale swirl, similar to that observed for $d > \sigma_d$ in figure 20, with the streamwise shift noted. In the same manner, the primary phenomenon for $p > \sigma_p$ is a saddle point with the flow above it resembling a sweep-ejection transition, consistent with the trends observed for $d < -\sigma_d$. It should be noted that formation of a pressure maximum at the sweep to ejection transition has been observed in several prior studies, e.g. Kim (1983, 1989), Kobashi & Ichijo (1986), Ghaemi & Scarano (2013), Joshi *et al.* (2014), and Naka *et al.* (2015).

There are a few more notable trends. First, for all velocity components, the correlation peaks associated with $p > \sigma_p$ are higher than those of $p < -\sigma_p$, also in agreement with corresponding deformation–velocity correlations. Second, the magnitude of the $R_{p,u}|_{p<-\sigma p}$ (figure 23*a*) peak is stronger under the 'vortex' than that above it, presumably since the horizontal velocity in regions located close to the wall is constructively influenced by the 'image vortex' on the other side of the surface. Third, the distribution of $R_{p,w}|_{p<-\sigma p}$ (figure 23*e*) depicts an anti-splatting flow, but the magnitudes are low, and that of $R_{p,w}|_{p>\sigma p}$ (figure 23*f*) appears like a splatting flow, with correlation magnitudes that are twice as high. The main difference between deformation–velocity and pressure–velocity correlations is the height of the peak. In the deformation–velocity correlations (figure 20), the centre of the swirl for $d > \sigma_d$ is located at $\Delta y/h \sim 0.11$, whereas the swirl centre for $p < -\sigma_p$ and the saddle point at the centre of the $p > \sigma_p$ plot shift upward with the pressure conditioning point. For example, figure 24 provides the pressure–wall-normal velocity correlation and conditionally sampled streamlines for pressure measured at $y/h = 0.2$, showing similar flow features shifted to a higher elevation, and an increasing distance between positive and negative correlation peaks. The latter trend is expected due to increase in
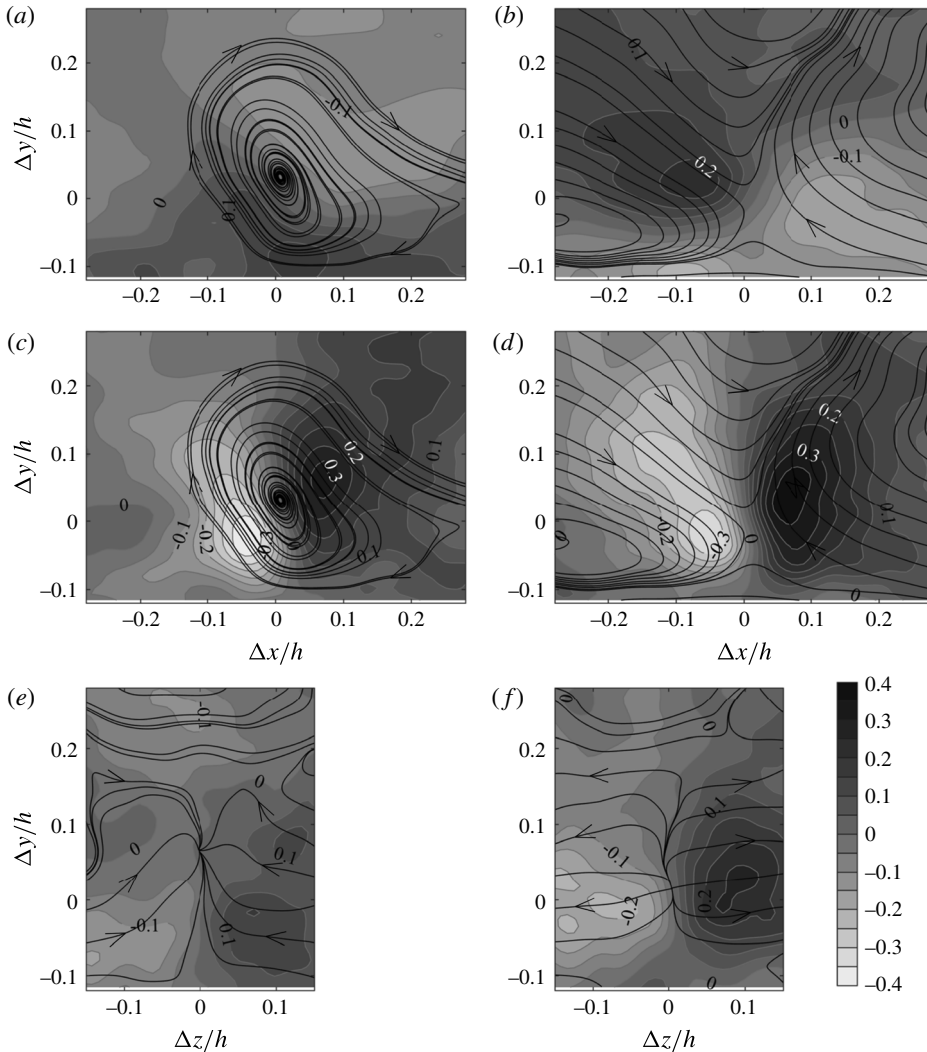
FIGURE 23. The pressure–velocity conditional correlations, based on the pressure at $y = 0.12h$: (*a*) $R_{p,u}|_{p<-\sigma p}$, (*b*) $R_{p,u}|_{p>\sigma p}$, (*c*) $R_{p,v}|_{p<-\sigma p}$, (*d*) $R_{p,v}|_{p>\sigma p}$, (*e*) $R_{p,w}|_{p<-\sigma p}$ and (*f*) $R_{p,w}|_{p>\sigma p}$. In (*a*–*d*) $\Delta z = 0$ and in (*e*,*f*) $\Delta x = 0$.

the size of characteristic eddies with distance from the wall (Townsend 1976; Perry & Chong 1982).

The conditional correlations between deformation and vorticity components have been calculated in order to further characterize flow structures associated with the deformation. Figure 25(*a*,*b*) show the deformation–spanwise vorticity correlations conditioned on $d > \sigma_d(R_{d,\omega z'}|_{d>\sigma d})$ and $d < -\sigma_d(R_{d,\omega z'}|_{d<-\sigma d})$, respectively. The peak of $R_{d,\omega z'}|_{d>\sigma d}$ is located at $\Delta x/h \approx 0.1$ and $\Delta y/h \approx 0.1$, very close to the centre of the spiral streamlines in figure 20(*a*,*c*) and the pressure–deformation correlation peak (figure 14*a*). It is characterized by negative correlation values, suggesting that the bump is located preferentially behind/upstream of a region of negative spanwise vorticity fluctuation. To determine whether this vorticity is indeed associated with
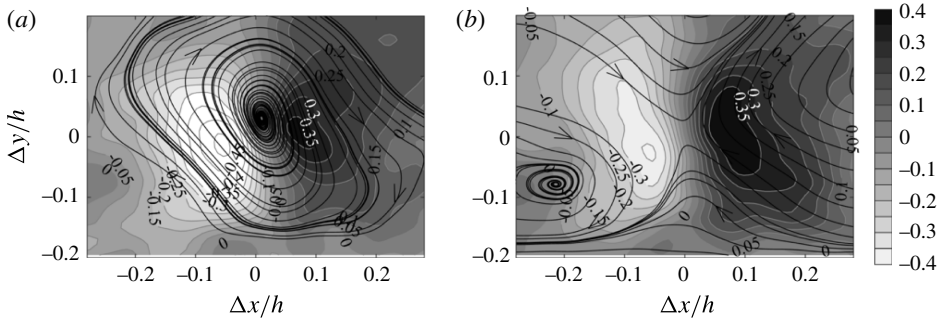
FIGURE 24. Distributions of pressure–wall-normal velocity conditional correlations on the $\Delta z = 0$ plane, based on the pressure at $(0, 0.2h, 0)$: (a) $R_{p,v}|_{p<-\sigma p}$; (b) $R_{p,v}|_{p>\sigma p}$. Streamlines show the corresponding conditionally averaged flow field.
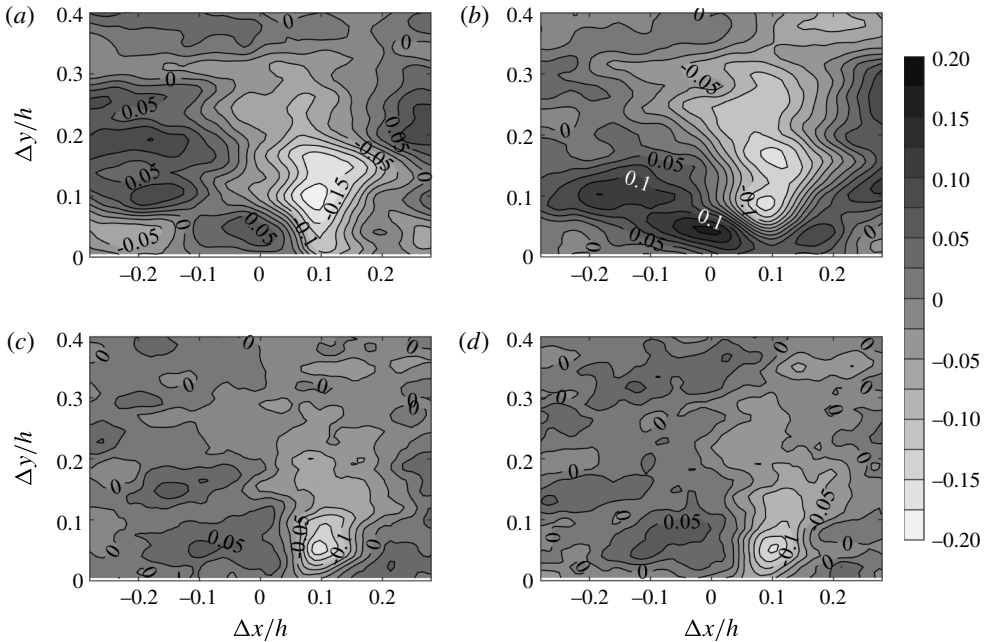

FIGURE 25. (a,b) Conditional deformation–spanwise vorticity correlations and (c,d) corresponding deformation-λ_2 correlations: (a) $R_{d,\omega z'}|_{d>\sigma d}$, (b) $R_{d,\omega z'}|_{d<-\sigma d}$, (c) $R_{d,\lambda 2}|_{d>\sigma d}$ and (d) $R_{d,\lambda 2}|_{d<-\sigma d}$.

vortices, we also calculate the distribution of the conditional correlation between deformation and λ_2, which is a popular method for identifying vortices introduced by Jeong & Hussain (1995). Results for $d > \sigma_d$, presented in figure 25(c), show that $\Delta x/h \approx 0.1$ is characterized by negative values of λ_2, confirming the preferred presence of a vortex. Distributions of $R_{d,\omega z'}|_{d>\sigma d}$ in an x–z plane for $\Delta y/h = 0.1$ (figure 26a) indicate the correlation peaks near $\Delta z = 0$, but it has a broad spanwise extent. Hence, the ejection regions above bumps are preferentially associated with negative spanwise vortices located downstream of the positive deformation. For negative deformations, figure 25(b) shows a region of preferentially positive ω_z', also
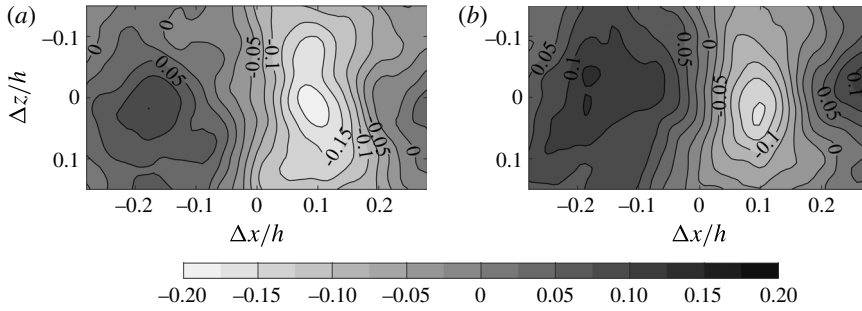
FIGURE 26. Conditional deformation–spanwise vorticity correlations in an x–z plane located at $\Delta y/h = 0.1$: (a) $R_{d,\omega z'}|_{d>\sigma d}$; (b) $R_{d,\omega z'}|_{d<-\sigma d}$.
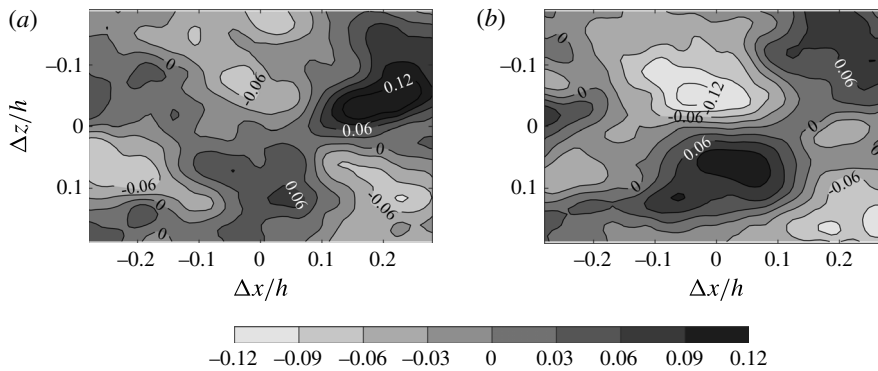

FIGURE 27. Conditional deformation–streamwise vorticity correlations in an x–z plane located at $\Delta y/h = 0.08$: (a) $R_{d,\omega x'}|_{d>\sigma d}$; (b) $R_{d,\omega x'}|_{d<-\sigma d}$.

at $\Delta x/h \approx 0.1$ and $\Delta y/h \approx 0.1$. However, the corresponding values of $R_{d,\lambda 2}|_{d<-\sigma d}$ at $\Delta x/h \sim 0.1$, which are presented in figure 25(d), are negative. Hence, λ_2 is preferentially positive, i.e. the dimples are not associated with the presence of vortices, consistent with the shape of streamlines presented (figure 20). This observation indicates that the $\omega_z' > 0$ region at the sweep-ejection transition around $\Delta x/h = 0.1$ is associated with low vorticity magnitude. It is presumably caused by a decrease in near-wall velocity gradients as the flow is slowing down under the influence of adverse pressure gradients, culminating with separation/ejection. The spanwise extent of this low-velocity-gradient region is broad, as demonstrated by the x–z distribution of $R_{d,\omega z'}|_{d<-\sigma d}$ presented in figure 26(b).

The conditional correlations between deformation and streamwise vorticity based on large positive ($R_{d,\omega x'}|_{d>\sigma d}$) and negative ($R_{d,\omega x'}|_{d<-\sigma d}$) deformations are shown in figure 27(a,b), respectively. Results are presented in an x–z plane located at $\Delta y/h = 0.08$, which is the elevation where the correlation magnitudes peak. Distributions in other nearby elevations have similar shapes (not shown). In both cases, correlation extrema with low magnitudes are preferentially located in a different spanwise plane relative to the deformation conditioning point. The two correlation peaks with opposite signs at $-0.1 < \Delta x/h < 0.1$ in figure 27(a) indicate that bumps are preferentially developed in regions where the streamwise-vortex-induced wall-normal velocity is positive (ejections). Further downstream, at $\Delta x/h > 0.1$, the correlation
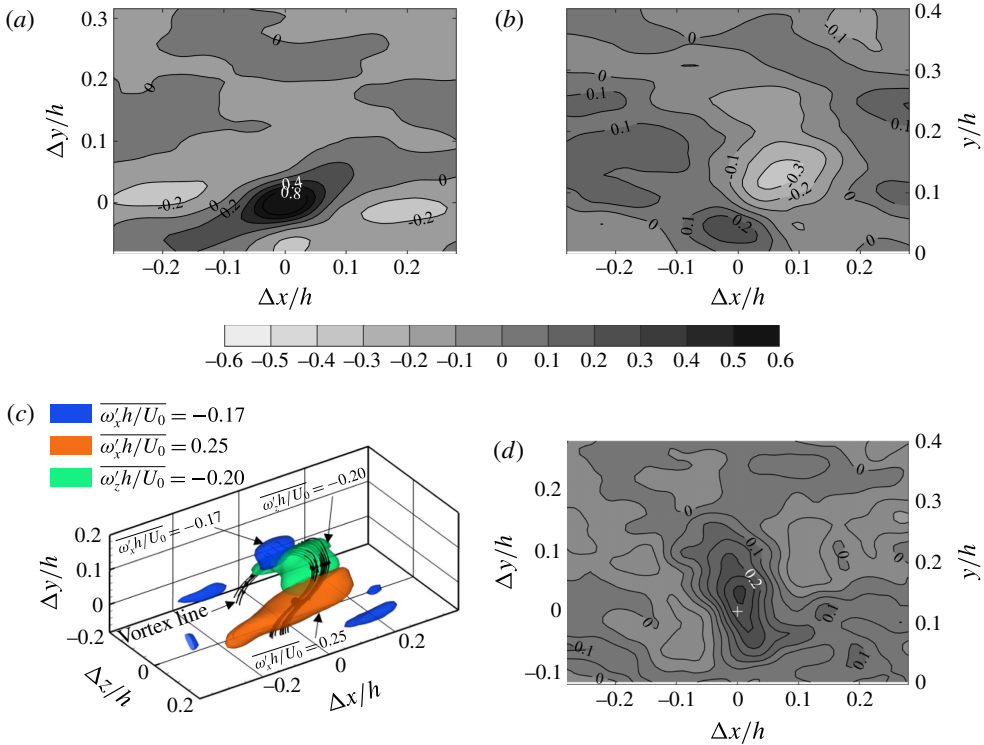
FIGURE 28. (*a–c*) Results of analysis conditioned on $d(0, 0) > \sigma_d$ and $\omega'_x(0, 0.08h, 0.05h) > 0$: (*a*) d–ω'_x correlation in the $\Delta z/h = 0.05$ plane; (*b*) d–ω'_z correlation at $\Delta z/h = 0$; (*c*) iso-surfaces of $\overline{\omega'_x h/U_0} = -0.17$, $= 0.25$ and $\overline{\omega'_z h/U_0} = -0.20$, along with the corresponding vortex lines; and (*d*) pressure–spanwise vorticity correlation conditioned on $p < -\sigma_p$ (at $y = 0.12h$, as indicated by a +) in the $\Delta z = 0$ plane.

extrema have opposite signs, consistent with a sweeping motion. As demonstrated later, and consistent with the spanwise vortex at $\Delta x/h \sim 0.1$ (figures 25a and 26a), the bumps preferentially form under and upstream of the head of a hairpin vortex.

This relationship between ω'_x, ω'_z, and positive deformation is further investigated by calculating the deformation–vorticity correlations, conditioned on both $d(0, 0) > \sigma_d$, and $\omega'_x(0, 0.08h, 0.05h) > 0$. Results for d–ω'_x correlation in the $\Delta z/h = 0.05$ plane is presented in figure 28(*a*), and that for d–ω'_z in the $\Delta z/h = 0$ plane in figure 28(*b*). The vertical coordinates are expressed both in terms of $\Delta y/h$ and y/h. The fact that the d–ω'_x correlation peaks at the conditioning point is not meaningful because the positive values are imposed. However, figure 28(*a*) also shows an inclined layer of elevated correlations extending from both sides of the peak having the familiar angle of 15°–20° (exact value depends on the criterion used) with the horizontal direction. The same angle has been seen for $R_{u,u}$ in many studies (e.g. Kim 1989; Liu, Adrian & Hanratiy 2001; Hutchins & Marusic 2007*b*; Wu & Christensen 2010; Ghaemi & Scarano 2013; Sillero, Jiménez & Moser 2014), and have been attributed to hairpin vortices (Adrian, Meinhart & Tomkins 2000). Furthermore, figure 28(*b*) shows a region of high correlation with negative spanwise vorticity downstream, above and spanwise offset from the ω'_x conditioning point. The elevation of this peak, $y/h = 0.13$, falls within the broad minimum in figure 25(*a*) (both are conditioned on $d > \sigma_d$), but

adding the offset ω'_x constraint increases the d–ω'_z correlation peak magnitude by $\sim 100\,\%$. Hence, the elevated d–ω'_x correlation appears to be a leg of a hairpin vortex, and the d–ω'_z correlation peak is the head of this vortex. Additional confirmation can be obtained by plotting the conditionally averaged flow field under the same conditions. Figure 28(*c*) shows iso-surfaces of $\overline{\omega'_x h/U_0} = -0.17$ and 0.25, as well as $\overline{\omega'_z h/U_0} = -0.2$ in different colours (overbar indicates conditionally averaged variable). It confirms the preferred presence of an inclined quasi-streamwise vortex as well as a counter-rotating (negative) vortex on the other side of the deformation, located at a distance of $\Delta z = 0.15h(\Delta z^+ = 350)$ from the conditioning point. It also shows the region with high $\overline{\omega'_z h/U_0}$ at the head of the hairpin. Finally, figure 28(*c*) also shows several conditionally averaged vortex lines originating from the vicinity of the vorticity conditioning point, passing through the hairpin head, and turning back into the other leg. Clearly, the positive deformation is located upstream of a negative spanwise vortex and flanked by streamwise vortices of opposite signs, consistent with the features of a hairpin-like structure. If the analysis is repeated by imposing $\omega'_x(0, 0.08h, -0.05h) < 0$, the 3D depiction appears to be quite similar (not shown) except for a swap in the size of the iso-surfaces of $\overline{\omega'_x h/U_0}$, corresponding to the location of the conditioning point. The picture becomes complete by plotting the distribution of pressure–spanwise vorticity correlation, conditioned on $p(0, 0.12h, 0) < -\sigma_p$ in figure 28(*d*). It shows that the pressure minimum is located in the same streamwise plane but slightly below the negative spanwise vorticity peak, and falls within the broad deformation–pressure correlation peak in figure 14(*a*). Hence, the pressure minimum preferentially causing the bump upstream of the hairpin head is located slightly below the point of peak spanwise vorticity. Such a vertical offset between the locations of pressure and spanwise vorticity minima in a hairpin structure is consistent with trends reported by Ghaemi & Scarano (2013). Their measurements focus on the $y^+ < 149$ region, and show a distance of $\Delta z^+ \approx 80$ between the hairpin legs, and the present observations extend to higher elevation with the corresponding larger distance between legs.

For negative deformations, we have already established that there is no spanwise vortex in front of dimples in the vicinity of the d–ω'_z correlation peak (figure 25*b*,*d*). The pressure maximum causing this dimple is preferentially associated with a transition between sweep and ejection (figure 23*b*,*d*). The positive spanwise vorticity fluctuation ahead of the dimple is located in the ejection region, where the averaged vorticity is lower than the mean (negative) value. As illustrated in numerous papers, for example, Kim (1983, 1989), Kobashi & Ichijo (1986), Chang, Piomelli & Blake (1999), Ghaemi & Scarano (2013), Joshi *et al.* (2014) and Naka *et al.* (2015), an inclined shear layer forms at the interface between an upstream sweep to a downstream ejection. The vicinity of the origin of this layer is shown in figures 20(*b*) and 23(*b*), and a more extended view is evident from the conditionally average pressure distribution and streamlines presented in figure 29 for $p(0, 0.02h, 0) > \sigma_p$. Inclination of this shear layer might be contributing to the (hydrodynamically induced) streamwise phase lag between dimples and the positive pressure fluctuations at $y/h > 0.12$, the location of peak correlation (figure 14*c*,*d*). In addition, the correlation peaks at $-0.1 < \Delta x/h < 0.1$ in figure 27(*b*) indicate that dimples preferentially form in regions with streamwise-vortex-induced downward sweeping flows. Such a phenomenon is not necessarily associated with sweep-ejection transition. However, as figure 27(*b*) shows, the deformation–streamwise vorticity correlation sign changes at $\Delta x/h > 0.1$. Such a change might occur, for example, at a sweep-ejection transition, where the direction of velocity fluctuation changes abruptly.
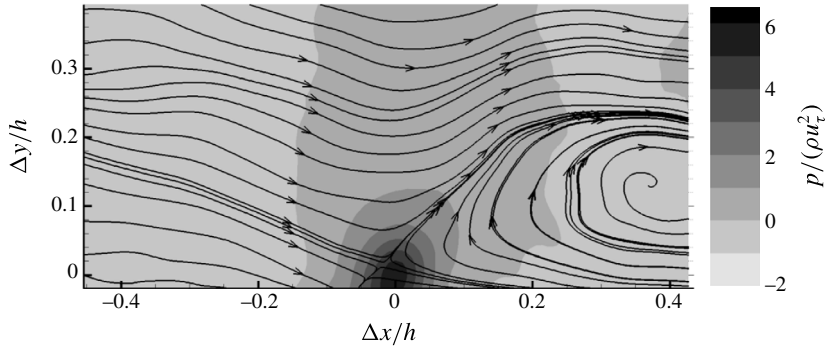
FIGURE 29. The conditionally averaged pressure distribution and streamlines, based on $p(0, 0.02h, 0) > \sigma_p$.

4. Summary and concluding remarks

The effect of a turbulent channel flow on deformation of a compliant wall is investigated experimentally using simultaneous time-resolved TPIV to measure the 3D flow and MZI to map the distribution of surface deformation. As summarized in appendix B, the TPIV data is used for determining the pressure distributions by calculating the spatial distribution of material acceleration and integrating it spatially. In a separate experiment MZI alone is used for mapping the wall shape for a larger FOV. The present PDMS wall could be characterized as 'stiff' because its shear speed (17 m s^{-1}) is much higher than the channel centreline velocity (2.5 m s^{-1}). Hence, after detrending and filtering out the channel vibrations, the amplitudes of wall deformations are much smaller than the wall unit, resulting in one-way coupling between the flow and the wall. Accordingly, the profiles of mean velocity and Reynolds stresses are consistent with those of typical turbulent channel flows.

The surface dynamics consist of several components. The low-frequency ($\omega h/U_0 < 1.6$) part does not appear to travel with the flow. At higher frequencies, two deformation advection speeds are prevalent. The 'fast' mode travels at U_0, and has a characteristic length scale of approximately $1.9h$. This mode is larger than the FOV of the combined TPIV/MZI experiment, and is only captured by the MZI measurements with a large FOV. Based on the Chase (1991) model, which is described in appendix A, a stiff compliant wall is most sensitive to pressure perturbations with a wavelength of approximately three times the coating thickness. In the present study, this length scale happens to corresponds to $\sim 1.9h$, consistent with measured wavelength of the fast mode. Hence, one could tune the compliant surface response and match it with desired flow features by varying its thickness. For the present conditions, the advected response of the wall to boundary layer turbulent structures occurs at a 'slow' mode, which travels at $0.72U_0$ based on the slope of the wavenumber–frequency spectra, and has a length scale approximately $0.5h$. The spatial conditional correlations between deformation and pressure peak at $y/h \sim 0.12$ ($y^+ \sim 280$) for bumps and ~ 0.14 for dimples, where the mean flow velocity ($\sim 0.77U_0$) is only slightly higher than the speed of the slow mode. Hence, turbulent structures at this elevation, which are located in the log-layer, and correspond to the peak in Reynolds shear stress and the end of the plateau in the streamwise velocity fluctuations, have dominant effects on the wall deformation. The $\langle u'u' \rangle/u_\tau$ plateau has been attributed to large-scale motions in the outer part of the boundary layer
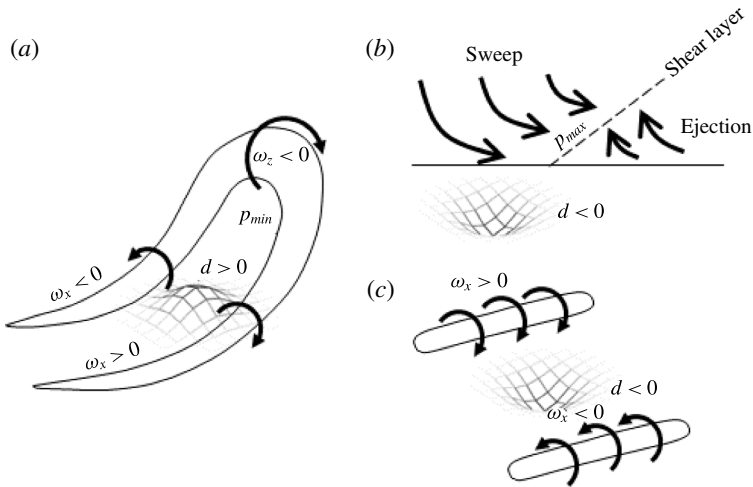
FIGURE 30. Conceptual models for the relationships between coherent flow structure and wall deformation: (*a*) a bump formed between the legs of a hair pin vortex; (*b*) a dimple forming at the transition between a sweep and an ejection; and (*c*) negative deformations on the sweeping side of streamwise vortices.

(Marusic *et al.* 2010; Hultmark 2012). However, the pressure–deformation cross-spectra show that the surface response to turbulent pressure fluctuations is broad, and the range of scales involved expands to higher wavenumbers with decreasing distance from the wall.

The spatial correlation peak shows a streamwise phase lag between deformation and pressure at $y/h \sim 0.12$. For the present conditions, only a small fraction of this offset ($\sim 24\%$) is attributed to the viscoelastic damping by the material, as predicted from the Chase (1991) model. This contribution is weakly dependent on the material loss tangent, and decreases slightly with increasing frequency. Most of the offset ($\sim 76\%$) is associated with variations of pressure phase with elevations, namely a phase lag of the near-wall pressure relative to that in the log-layer. This lag is evident both in the spatial two-point correlation of pressure, which is inclined slightly, and the corresponding cross-spectra. Both the material and hydrodynamic phase lags should be accounted for while developing flow control strategies involving compliant surfaces. It should be noted that phase lags between near-wall small-scale structures and log-layer turbulence have been reported before based on velocity measurements (e.g. Mathis *et al.* 2011; Ganapathisubramani *et al.* 2012).

A series of conditional correlations are used for identifying flow structures affecting the formation of bumps and dimples on the surface. The spatial relationships between the flow and deformation field are summarized in conceptual models shown in figure 30. The bumps are preferentially situated in ejection regions upstream of log-layer negative spanwise vortices, and pressure minima located slightly below the vortex centre (figure 30*a*). When the conditional correlation includes streamwise vorticity, the 3D flow phenomenon involved appears like a hairpin vortex, with the bump being flanked by quasi-streamwise vortices, below and behind the hairpin head. Conversely, the dimples are preferentially associated with pressure maxima developing at the transition between sweep and ejection regions (figure 30*b*). The phase lag is

attributed to the inclination of the shear layer at the sweep-ejection interface. Dimples also form on the sweeping flow side of streamwise vortices (figure 30*c*).

Although the Chase (1991) model, as it is presently implemented (see appendix A), is two-dimensional and has an infinite domain, using it has been instrumental for (i) elucidating the frequency spectrum of the deformation, (ii) quantifying the contribution of material damping on the deformation–pressure phase lag, (iii) highlighting the effect of varying the wall thickness on the wavelength of peak response for stiff materials, and the frequency of peak response at low wavenumbers, and (iv) showing that for the present conditions, the effect of shear stresses is much smaller than that of the pressure. Finally, the frequency–wavenumber spectrum obtained from this model provides insightful guidance in selecting flow and compliant wall parameters for future research. For example, to increase the wall response to pressure fluctuations, one has to match the shear speed of the wall with that of either the mean flow speed or with the velocity at an elevation where the turbulence parameters have the highest correlation with the wall deformation. Conversely, to explain and elucidate for non-advected parts of the measured deformation, one would have to account for the three dimensionality of stress/strain field within the compliant wall, including the effects of its finite boundaries.

Acknowledgements

Supplementary movies

Supplementary movies are available at https://doi.org/10.1017/jfm.2017.299.

Appendix A. The Chase (1991) model

This appendix summarizes our implementation of the Chase (1991) classical model of the response of a viscoelastic layer to fluctuating pressure and wall shear stresses, because of its significance to interpretation of the present data. The geometry of the infinitely large compliant layer is two-dimensional, with only streamwise and wall-normal deformation components, denoted as $d_x(x, y, t)$ and $d_y(x, y, t)$, respectively. In the rest of this paper we use $d = d_y(x, y = 0, t)$ to describe the surface deformation. The prescribed 1D pressure and shear waves at the interface with the fluid are $p_0 \exp[i(kx - \omega t)]$ and $\tau_0 \exp[i(kx - \omega t)]$, respectively, where p_0 and τ_0 represent small wave amplitudes. The material behaviour is modelled using the Navier equation for an elastic material (Landau & Lifshitz 1970):

$$\rho_c \frac{\partial^2 \boldsymbol{d}}{\partial t^2} = \frac{E}{2(1 + \sigma)} \nabla^2 \boldsymbol{d} + \frac{E}{2(1 + \sigma)(1 - 2\sigma)} \nabla(\nabla \cdot \boldsymbol{d}), \tag{A 1}$$

where $\boldsymbol{d} = d_x \boldsymbol{i} + d_y \boldsymbol{j}$ is the displacement vector (boldface denotes a vector), ρ_c is the material density, σ is the Poisson's ratio and E is the Young's modulus. Viscoelasticity is accounted for by replacing E with a complex modulus $\tilde{E} = E' + iE''$, introducing the loss tangent, $\zeta = E''/E'$. The wall deformation is solved by expressing the $\boldsymbol{d}$ in terms

of a scalar potential, φ, and a vector potential, ψ, using the Helmholtz decomposition,

$$d_x = \frac{\partial \varphi}{\partial x} + \frac{\partial \psi}{\partial y}; \quad d_y = \frac{\partial \varphi}{\partial y} - \frac{\partial \psi}{\partial x}. \tag{A 2a,b}$$

Substituting (A 2) into (A 1), one can show that both φ and ψ are solutions of the wave equation with complex wave speeds, c_l and c_t, respectively. Their relations to the material properties are

$$\left.\begin{aligned} c_l &= \sqrt{\frac{E(1-\sigma)}{\rho(1+\sigma)(1-2\sigma)}} \\ c_t &= \sqrt{\frac{E}{2\rho(1+\sigma)}}. \end{aligned}\right\} \tag{A 3}$$

The solutions to the wave equations are

$$\left.\begin{aligned} \varphi(x, y, t) &= \hat{\varphi}(y)e^{i(kx-\omega t)} \\ \psi(x, y, t) &= \hat{\psi}(y)e^{i(kx-\omega t)}, \end{aligned}\right\} \tag{A 4}$$

with amplitudes

$$\left.\begin{aligned} \hat{\varphi}(y) &= a_l \sinh[K_l(y+l_0)] + b_l \cosh[K_l(y+l_0)] \\ \hat{\psi}(y) &= a_t \sinh[K_t(y+l_0)] + b_t \cosh[K_t(y+l_0)]. \end{aligned}\right\} \tag{A 5}$$

Here, $K_l = (k^2 - \omega^2/c_l^2)^{1/2}$ and $K_t = (k^2 - \omega^2/c_t^2)^{1/2}$. The four unknown constants, a_l, b_l, a_t and b_t, are determined based on the boundary conditions. At the interface with the fluid ($y = 0$), the normal and shear stresses, σ_{yy} and σ_{xy}, are

$$\left.\begin{aligned} \sigma_{yy}(y=0) &= [-p_0 + i\omega d_y(y=0)z_+]e^{i(kx-\omega t)} \\ \sigma_{xy}(y=0) &= \tau_0 e^{i(kx-\omega t)}, \end{aligned}\right\} \tag{A 6}$$

where z_+ is the acoustic impedance of the liquid, which accounts for the fluid loading. Assuming that the bottom surface is rigid, $d_x(x, -l_0, t) = d_y(x, -l_0, t) = 0$. A MATLAB code has been written to calculate the amplitudes of pressure and shear-induced deformations. To validate that the model is implemented correctly, we have repeated all calculations discussed in Chase (1991), and compared them to those provided in the original plots, including cases with non-rigid bottom boundary conditions. The results agree to the precision possible by digitizing the original plots. Subsequently, the MATLAB code has been used to calculate the wavenumber–frequency spectrum provided in figure 11 for pressure perturbation. The corresponding response to shear only has also been calculated. The wavenumber–frequency distribution of the ratio between pressure-induced and shear-induced deformation in response to excitation with the same amplitude ($p_0 = \tau_0$) is presented in figure 31. Clearly, the compliant surface is much more sensitive to the pressure perturbations in the wavenumber and frequency ranges relevant to the present study. Hence, the effect of shear stresses on the surface deformation is neglected.
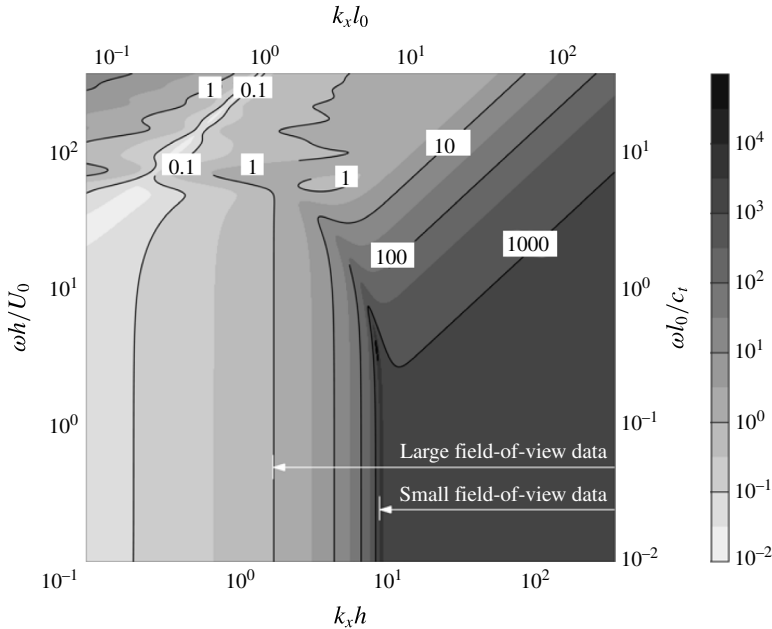
FIGURE 31. The ratio between deformation amplitudes in response to pressure and shear perturbations of equal amplitudes, as predicted by the Chase (1991) model.

Appendix B. Calculation of pressure field

The instantaneous pressure field is spatially integrated from its gradient, $\nabla p = -\rho(\mathrm{D}\boldsymbol{u}/\mathrm{D}t - \nu\nabla^2\boldsymbol{u})$, using the measured velocity distributions to calculate the material acceleration ($\mathrm{D}\boldsymbol{u}/\mathrm{D}t$). Although calculated to determine its magnitude/influence, the viscous diffusion term is neglected since it is typically several orders of magnitude smaller than the instantaneous material acceleration. The pressure reconstruction involves two steps, i.e. calculation of material acceleration and pressure integration. As discussed in Liu & Katz (2013) and de Kat & van Oudheusden (2010), the material acceleration at time t_n is calculated from five consecutive 3D particle distributions I_{n-2}, I_{n-1}, I_n, I_{n+1}, I_{n+2} recorded at times t_{n-2}, t_{n-1}, t_n, t_{n+1}, t_{n+2}, respectively, which are separated by a constant time interval Δt. The positions of a group of particles located around $\boldsymbol{x}_n$ at t_n, in frames recorded at t_{n-1} and t_{n+1} are calculated, using TPIV, from the corresponding displacement vectors, $\boldsymbol{D}_{n,n-1}(\boldsymbol{x}_n)$ and $\boldsymbol{D}_{n,n+1}(\boldsymbol{x}_n)$. Using the same initial instant and location, as defined by the first subscript, and calculating the displacements both forward and backward in time assure that the procedure follows the motion of the same particle group. In other words, the interrogation volume at t_n remains at $\boldsymbol{x}_n$ for both calculations, and displaced to $\boldsymbol{x}_n + \boldsymbol{D}_{n,n-1}$ at t_{n-1} and to $\boldsymbol{x}_n + \boldsymbol{D}_{n,n+1}$ at t_{n+1}. The velocity of this particle group at t_n is estimated using second-order central differencing, namely $\boldsymbol{u}_n \approx [\boldsymbol{D}_{n,n+1}(\boldsymbol{x}_n) - \boldsymbol{D}_{n,n-1}(\boldsymbol{x}_n)]/(2\Delta t)$. The corresponding material acceleration is estimated from

$$\mathrm{D}\boldsymbol{u}/\mathrm{D}t(\boldsymbol{x}_n, t_n) \approx [\boldsymbol{u}_{n+1}(\boldsymbol{x}_n + \boldsymbol{D}_{n,n+1}, t_{n+1}) - \boldsymbol{u}_{n-1}(\boldsymbol{x}_n + \boldsymbol{D}_{n,n-1}, t_{n-1})]/(2\Delta t). \quad \text{(B 1)}$$

Since the particle displacement between exposures involves a fraction of the vector spacing, the velocity at $\boldsymbol{x}_n + \boldsymbol{D}_{n,n-1}$ and $\boldsymbol{x}_n + \boldsymbol{D}_{n,n+1}$ is obtained using tri-cubic interpolation of values calculated at the regular TPIV grid points.

To spatially integrate the material acceleration, we have developed a GPU-based 3D virtual-boundary omni-directional integration method, extending the 2D procedures described in Liu & Katz (2013). To minimize effects of errors occurring along certain integration path, the pressure at every point is determined based on spatial integration from the boundaries in all directions, and averaging results obtained for all paths. To prevent directional bias, the integration starts from uniformly distributed points on the surface of a sphere surrounding the sample volume, and proceeds along parallel lines in all directions, from one surface grid point to all the others. A similar integration procedure is described in Liu, Moreto & Siddle-Mitchell (2016). To obtain the pressure on the boundary for the initial iteration, we start at a certain point and integrate the pressure gradients (acceleration) over the surface. Subsequently, the surface values are updated based on the results of 3D omni-directional integration. The corrected values are used in the next iteration, and the process is repeated, typically requiring two iterations to achieve converged values. Further reduction in errors can be achieved by avoiding (circumventing) regions where the acceleration errors are particularly high. These regions can be readily identified based on local closed-loop integration of material acceleration. Due to the large number of integration paths involved, the omni-directional integration procedure is implemented on a Tesla K40c GPU board. It reduces the processing time of one instantaneous realization from approximately 6 h on a quad-core personal computer to approximately 2 min.

An alternative approach for calculating the pressure is based on solving the pressure Poisson equation, which requires the estimation of the second-order derivative of the velocity, along with proper combination of Neumann and/or Dirichlet-type boundary conditions (e.g. Baur & Köngeter 1999; Gurka *et al.* 1999; Koschatzky *et al.* 2011; Ghaemi *et al.* 2012; de Kat & van Oudheusden 2012; Ghaemi & Scarano 2013). Different approaches for calculating pressure have been compared by Charonko *et al.* (2010) and reviewed by van Oudheusden (2013). Comparisons based on synthetic data have shown that in regions located away from the planes where the Dirichlet boundary conditions are imposed, results obtained from both approaches are essentially identical.

REFERENCES

ABE, H., MATSUO, Y. & KAWAMURA, H. 2005 A DNS study of Reynolds-number dependence on pressure fluctuations in a turbulent channel flow. In *TSFP Digital Library Online*. Begel House Inc.

ADRIAN, R. J., MEINHART, C. D. & TOMKINS, C. D. 2000 Vortex organization in the outer region of the turbulent boundary layer. *J. Fluid Mech.* **422**, 1–54.

ANTONIA, R. A. & LUXTON, R. E. 1971 The response of a turbulent boundary layer to a step change in surface roughness. Part 1. Smooth to rough. *J. Fluid Mech.* **48**, 721–761.

ATKINSON, C., COUDERT, S., FOUCAUT, J.-M., STANISLAS, M. & SORIA, J. 2011 The accuracy of tomographic particle image velocimetry for measurements of a turbulent boundary layer. *Exp. Fluids* **50**, 1031–1056.

ATKINSON, C. & SORIA, J. 2009 An efficient simultaneous reconstruction technique for tomographic particle image velocimetry. *Exp. Fluids* **47**, 553–568.

BAUR, T. & KÖNGETER, J. 1999 PIV with high temporal resolution for the determination of local pressure reductions from coherent turbulent phenomena. In *Proceedings of the 3rd International Workshop on Particle Image Velocimetry, Santa Barbara, USA*.

BENJAMIN, T. B. 1960 Effects of a flexible boundary on hydrodynamic stability. *J. Fluid Mech.* **9**, 513–532.

BENJAMIN, T. B. 1963 The threefold classification of unstable disturbances in flexible surfaces bounding inviscid flows. *J. Fluid Mech.* **16**, 436–450.

BERNARDINI, M., PIROZZOLI, S. & ORLANDI, P. 2014 Velocity statistics in turbulent channel flow up to $Re_\tau = 4000$. *J. Fluid Mech.* **742**, 171–191.

BLAKE, W. K. 1970 Turbulent boundary layer wall pressure fluctuations on smooth and rough walls. *J. Fluid Mech.* **44**, 637–660.

BLICK, E. F. & WALTERS, R. R. 1968 Turbulent boundary-layer characteristics of compliant surfaces. *J. Aircraft* **5** (1), 11–16.

BONE, D. J., BACHOR, H. A. & SANDEMAN, R. J. 1986 Fringe-pattern analysis using a 2-D Fourier transform. *Appl. Opt.* **25** (10), 1653–1660.

BULL, M. K. 1967 Wall-pressure fluctuations associated with subsonic turbulent boundary layer flow. *J. Fluid Mech.* **28** (4), 719–754.

BUSHNELL, D. M., HEFNER, J. N. & ASH, R. L. 1977 Effect of compliant wall motion on turbulent boundary layers. *Phys. Fluids* **20**, S31–S48.

CARPENTER, P. W. & GARRAD, A. D. 1985 The hydrodynamic stability of flows over Kramer-type compliant surfaces. Part 1. Tollmien–Schlichting instabilities. *J. Fluid Mech.* **155**, 465–510.

CARPENTER, P. W. & GARRAD, A. D. 1986 The hydrodynamic stability of flows over Kramer-type compliant surfaces. Part 2. Flow-induced surface instabilities. *J. Fluid Mech.* **170**, 199–232.

CASTELLINI, P., MARTARELLI, M. & TOMASINI, E. P. 2006 Laser Doppler vibrometry: development of advanced solutions answering to technology's needs. *Mech. Syst. Signal Process.* **20**, 1265–1285.

CHANG, P. A., PIOMELLI, U. & BLAKE, W. K. 1999 Relationship between wall pressure and velocity field sources. *Phys. Fluids* **11**, 3434–3448.

CHARONKO, J. J., KING, C. V., SMITH, B. L. & VLACHOS, P. P. 2010 Assessment of pressure field calculations from particle image velocimetry measurements. *Meas. Sci. Technol.* **21**, 105401.

CHASE, D. M. 1991 Generation of fluctuating normal stress in a viscoelastic layer by surface shear stress and pressure as in turbulent boundary-layer flow. *J. Acoust. Soc. Am.* **89** (6), 2589–2596.

CHOI, H. & MOIN, P. 1990 On the spacetime characteristics of wall-pressure fluctuations. *Phys. Fluids* **2** (8), 1450–1460.

CHOI, K.-S., YANG, X., CLAYTON, B. R., GLOVER, E. J., ATLAR, M., SEMENOV, B. N. & KULIK, V. M. 1997 Turbulent drag reduction using compliant surfaces. *Proc. R. Soc. Lond.* A **453**, 2229–2240.

CONTE, N. & JARDRET, V. 2002 Frequency specific characterization of very soft polymeric materials using nanoindentation testing. *Mat. Res. Soc. Symp. Proc.* **710**, DD7.10.1-6.

DEAN, R. B. 1978 Reynolds number dependence of skin friction and other bulk flow variables in two-dimensional rectangular duct flow. *Trans. ASME: J. Fluids Engng* **100**, 215–223.

DINKELACKER, A., HESSEL, M., MEIER, G. E. A. & SCHEWE, G. 1977 Investigation of pressure fluctuations beneath a turbulent boundary layer by means of an optical method. *Phys. Fluids* **20** (10), S216–S224.

DU, P., CHENG, C., LU, H. & ZHANG, X. 2013 Investigation of cellular contraction forces in the frequency domain using a PDMS micropillar-based force transducer. *J. Microelectromech. Syst.* **22** (1), 44–53.

DUNCAN, J. H. 1986 The response of an incompressible viscoelastic coating to pressure fluctuations in a turbulent boundary layer. *J. Fluid Mech.* **171**, 339–363.

DUNCAN, J. H., WAXMAN, A. M. & TULIN, M. P. 1985 The dynamics of waves at the interface between a viscoelastic coating and a fluid flow. *J. Fluid Mech.* **158**, 177.

ELSINGA, G. E., SCARANO, F., WIENEKE, B. & VAN OUDHEUSDEN, B. W. 2006 Tomographic particle image velocimetry. *Exp. Fluids* **41**, 933–947.

ENDO, T. & HIMENO, R. 2002 Direct numerical simulation of turbulent flow over a compliant surface. *J. Turbul.* **3**, 1–10.

FERRY, J. D. 1970 *Viscoelastic Properties of Polymers*. Wiley.

FISHER, D. H. & BLICK, E. F. 1966 Turbulent damping by flabby skins. *J. Aircraft* **3** (2), 163–164.

FITZGERALD, E. R. & FITZGERALD, J. W. 1998 Blubber and compliant coatings for drag reduction in fluids: V. Driving point shear impedance measurements on compliant surfaces. In *Proceedings of International Symp. on Seawater Drag Reduction 22–23 July, Newport, RI, USA* (ed. J. C. S. Meng), pp. 215–218.

FOUCAUT, J. M., CARLIER, J. & STANISLAS, M. 2004 PIV optimization for the study of turbulent flow using spectral analysis. *Meas. Sci. Technol.* **15**, 1046–1058.

FUNG, Y. C. 1965 *Foundations of Solid Mechanics*. Prentice Hall.

GAD-EL-HAK, M. 1986 The response of elastic and viscoelastic surfaces to a turbulent boundary layer. *Trans. ASME J. Appl. Mech.* **53**, 206–212.

GAD-EL-HAK, M. 1998 Compliant coatings: the simpler alternative. *Exp. Therm. Fluid Sci.* **16**, 141–156.

GAD-EL-HAK, M. 2002 Compliant coatings for drag reduction. *Prog. Aerosp. Sci.* **38**, 77–99.

GAD-EL-HAK, M., BLACKWELDER, R. F. & RILEY, J. J. 1984 On the interaction of compliant coatings with boundary layer flows. *J. Fluid Mech.* **140**, 257–280.

GANAPATHISUBRAMANI, B., HUTCHINS, N., MONTY, J. P., CHUNG, D. & MARUSIC, I. 2012 Amplitude and frequency modulation in wall turbulence. *J. Fluid Mech.* **712**, 61–91.

GHAEMI, S., RAGNI, D. & SCARANO, F. 2012 PIV-based pressure fluctuations in the turbulent boundary layer. *Exp. Fluids* **53** (6), 1823–1840.

GHAEMI, S. & SCARANO, F. 2013 Turbulent structure of high-amplitude pressure peaks within the turbulent boundary layer. *J. Fluid Mech.* **735**, 381–426.

GHIGLIA, D. C., MASTIN, G. A. & ROMERO, L. A. 1987 Cellular-automata method for phase unwrapping. *J. Opt. Soc. Am.* A **4** (1), 267–280.

GHIGLIA, D. C. & PRITT, M. D. 1998 *Two-Dimensional Phase Unwrapping*. Wiley.

GOLDSTEIN, R. M., ZEBKER, H. A. & WERNER, C. L. 1988 Satellite radar interferometry: two-dimensional phase unwrapping. *Radio Sci.* **23** (4), 713–720.

GRAHAM, J., KANOV, K., YANG, X. I. A., LEE, M. K., MALAYA, N., LALESCU, C. C., BURNS, R., EYINK, G., SZALAY, A., MOSER, R. D. & MENEVEAU, C. 2016 A web services-accessible database of turbulent channel flow and its use for testing a new integral wall model for LES. *J. Turbul.* **17** (2), 181–215.

GURKA, R., LIBERZON, A., HEFETZ, D., RUBINSTEIN, D. & SHAVIT, U. 1999 Computation of pressure distribution using PIV velocity data. In *Proceedings of the 3rd International Workshop on Particle Image Velocimetry, Santa Barbara, USA*.

HANSEN, R. J. & HUNSTON, D. L. 1974 An experimental study of turbulent flows over compliant surfaces. *J. Sound Vib.* **34**, 297–308.

HANSEN, R. J. & HUNSTON, D. L. 1983 Fluid-property effects on flow-generated waves on a compliant surface. *J. Fluid Mech.* **133**, 161–177.

HANSEN, R. J., HUNSTON, D. L., NI, C. C. & REISCHMAN, M. M. 1980 An experimental study of flow-generated waves on a flexible surface. *J. Sound Vib.* **68**, 317–334.

HARRIS, G. L. & LISSAMAN, P. B. S. 1969 Turbulent skin friction on compliant surfaces. *AIAA J.* **7** (8), 1625–1627.

HECHT, E. 2002 *Optics*, 4th edn. Addison-Wesley.

HESS, D. E., PEATTIE, R. A. & SCHWARZ, W. H. 1993 A noninvasive method for the measurement of flow-induced surface displacement of a compliant surface. *Exp. Fluids* **14**, 78–84.

HONG, J., KATZ, J., MENEVEAU, C. & SCHULTZ, M. P. 2012 Coherent structures and associated subgrid-scale energy transfer in a rough-wall turbulent channel flow. *J. Fluid Mech.* **712**, 92–128.

HONG, J., KATZ, J. & SCHULTZ, M. P. 2011 Near-wall turbulence statistics and flow structures over three-dimensional roughness in a turbulent channel flow. *J. Fluid Mech.* **667**, 1–37.

HOYAS, S. & JIMÉNEZ, J. 2006 Scaling of the velocity fluctuations in turbulent channels up to $Re_\tau = 2003$. *Phys. Fluids* **18** (1), 011702.

HULTMARK, M. 2012 A theory for the streamwise turbulent fluctuations in high Reynolds number pipe flow. *J. Fluid Mech.* **707**, 575–584.

HULTMARK, M., BAILEY, S. C. C. & SMITS, A. J. 2010 Scaling of near-wall turbulence in pipe flow. *J. Fluid Mech.* **649**, 103–113.

HUTCHINS, N. & MARUSIC, I. 2007a Large-scale influences in near-wall turbulence. *Phil. Trans. R. Soc. Lond.* **365**, 647–664.

HUTCHINS, N. & MARUSIC, I. 2007b Evidence of very long meandering features in the logarithmic region of turbulent boundary layers. *J. Fluid Mech.* **579**, 1–28.

ICHIOKA, Y. & INUIYA, M. 1972 Direct phase detecting system. *Appl. Opt.* **11** (7), 1507–1514.

ITOH, K. 1982 Analysis of the phase unwrapping algorithm. *Appl. Opt.* **21** (14), 2470.

JEON, S., CHOI, H., YOO, J. Y. & MOIN, P. 1999 Space-time characteristics of the wall shear-stress fluctuations in a low-Reynolds-number channel flow. *Phys. Fluids* **11** (10), 3084–3094.

JEONG, J. & HUSSAIN, F. 1995 On the identification of a vortex. *J. Fluid Mech.* **285**, 69–94.

JOSHI, P., LIU, X. & KATZ, J. 2014 Effect of mean and fluctuating pressure gradients on boundary layer turbulence. *J. Fluid Mech.* **748**, 36–84.

DE KAT, R. & VAN OUDHEUSDEN, B. W. 2010 Instantaneous planar pressure from PIV: analytic and experimental test-cases. In *15th International Symposium on Applications of Laser Techniques to Fluid Mechanics, Lisbon, Portugal, July 5–8.*

DE KAT, R. & VAN OUDHEUSDEN, B. W. 2012 Instantaneous planar pressure determination from PIV in turbulent flow. *Exp. Fluids* **52**, 1089–1106.

KIM, J. 1983 On the structure of wall bounded turbulent flows. *Phys. Fluids* **26**, 2088–2097.

KIM, J. 1989 On the structure of pressure fluctuations in simulated turbulent channel flow. *J. Fluid Mech.* **205**, 421–451.

KIM, E. & CHOI, H. 2014 Space-time characteristics of a compliant wall in a turbulent channel flow. *J. Fluid Mech.* **756**, 30–53.

KO, S. H. & SCHLOEMER, H. H. 1989 Calculations of turbulent boundary-layer pressure fluctuations transmitted into a viscoelastic layer. *J. Acoust. Soc. Am.* **85**, 1469–1477.

KOBASHI, Y. & ICHIJO, M. 1986 Wall pressure and its relation to turbulent structure of a boundary layer. *Exp. Fluids* **4**, 49–55.

KOSCHATZKY, V., MOORE, P. D., WESTERWEEL, J., SCARANO, F. & BOERSMA, B. J. 2011 High speed PIV applied to aerodynamic noise investigation. *Exp. Fluids* **50**, 863–876.

KRAMER, M. O. 1957 Boundary-layer stabilization by distributed damping. *J. Aero. Sci.* **24**, 459–460.

KRAMER, M. O. 1962 Boundary-layer stabilization by distributed damping. *Naval Engrs J.* **74** (2), 341–348.

KULIK, V. M., SEMENOV, B. N., BOIKO, A. V., SEOUDI, B. M., CHUN, H. H. & LEE, I. 2009 Measurement of dynamic properties of viscoelastic materials. *Exp. Mech.* **49**, 417–425.

LANDAHL, M. T. 1962 On the stability of a laminar incompressible boundary layer over a flexible surface. *J. Fluid Mech.* **13**, 609–632.

LANDAU, L. D. & LIFSHITZ, E. M. 1970 *Theory of Elasticity*, 2nd edn. Pergamon.

LEE, M. & MOSER, R. D. 2015 Direct numerical simulation of turbulent channel flow up to $Re_\tau \approx 5200$. *J. Fluid Mech.* **774**, 395–415.

LEE, T., FISHER, M. & SCHWARZ, W. H. 1993a Investigation of the stable interaction of a passive compliant surface with a turbulent boundary layer. *J. Fluid Mech.* **257**, 373–401.

LEE, T., FISHER, M. & SCHWARZ, W. H. 1993b The measurement of flow-induced surface displacement on a compliant surface by optical holographic interferometry. *Exp. Fluids* **14**, 159–168.

LEE, T., FISHER, M. & SCHWARZ, W. H. 1995 Investigation of the effects of a compliant surface on boundary-layer stability. *J. Fluid Mech.* **288**, 37–58.

LI, Y., PERLMAN, E., WAN, M., YANG, Y., MENEVEAU, C., BURNS, R., CHEN, S., SZALAY, A. & EYINK, G. L. 2008 A public turbulence database cluster and applications to study Lagrangian evolution of velocity increments in turbulence. *J. Turbul.* **9**, N31.

LIU, X. & KATZ, J. 2006 Instantaneous pressure and material acceleration measurements using a four-exposure PIV system. *Exp. Fluids* **41**, 227–240.

LIU, X. & KATZ, J. 2008 Cavitation phenomena occurring due to interaction of shear layer vortices with the trailing corner of a two-dimensional open cavity. *Phys. Fluids* **20**, 041702.

LIU, X. & KATZ, J. 2013 Vortex–corner interactions in a cavity shear layer elucidated by time-resolved measurements of the pressure field. *J. Fluid Mech.* **728**, 417–457.

LIU, X., MORETO, J. R. & SIDDLE-MITCHELL, S. 2016 Instantaneous pressure reconstruction from measured pressure gradient using rotating parallel ray method. In *54th AIAA Aerospace Sciences Meeting*. AIAA SciTech. *AIAA* 2016-1049.

LIU, Z., ADRIAN, R. J. & HANRATTY, T. J. 2001 Large-scale modes of turbulent channel flow: transport and structure. *J. Fluid Mech.* **448**, 53–80.

LOZANO-DURÁN, A. & JIMÉNEZ, J. 2014 Effect of the computational domain on direct simulations of turbulent channels up to $Re_\tau = 4200$. *Phys. Fluids* **26** (1), 011702.

LUHAR, M., SHARMA, A. S. & MCKEON, B. J. 2015 A framework for studying the effect of compliant surfaces on wall turbulence. *J. Fluid Mech.* **768**, 415–441.

MARK, J. E. (Ed.) 1999 *Polymer Data Handbook*. Oxford University Press.

MARUSIC, I., MATHIS, R. & HUTCHINS, N. 2010 High Reynolds number effects in wall turbulence. *Intl J. Heat Fluid Flow* **31**, 418–428.

MATHIS, R., HUTCHINS, N. & MARUSIC, I. 2009 Large-scale amplitude modulation of the small-scale structures in turbulent boundary layers. *J. Fluid Mech.* **628**, 311–337.

MATHIS, R., HUTCHINS, N. & MARUSIC, I. 2011 A predictive inner–outer model for streamwise turbulence statistics in wall-bounded flows. *J. Fluid Mech.* **681**, 537–566.

MCKEON, B. J. & SHARMA, A. S. 2010 A critical-layer framework for turbulent pipe flow. *J. Fluid Mech.* **658**, 336–382.

MCMICHAEL, J. M., KLEBANOFF, P. S. & MEASE, N. E. 1980 Experimental investigation of drag on a compliant surface. In *Viscous Flow Drag Reduction* (ed. G. R. Hough), vol. 72, pp. 410–438. AIAA.

MEINHART, C. D., WERELEY, S. T. & SANTIAGO, J. G. 2000 A PIV algorithm for estimating time-averaged velocity fields. *Trans. ASME J. Fluids Engng* **122**, 285–289.

MOFFAT, R. J. 1988 Describing the uncertainties in experimental results. *Exp. Therm. Fluid Sci.* **1**, 3–17.

MONTY, J. P. 2005 Developments in smooth wall turbulent duct flows. PhD thesis, the University of Melbourne.

NAKA, Y., STANISLAS, M., FOUCAUT, J., COUDERT, S., LAVAL, J. & OBI, S. 2015 Space-time pressure-velocity correlations in a turbulent boundary layer. *J. Fluid Mech.* **771**, 624–675.

VAN OUDHEUSDEN, B. W. 2013 PIV-based pressure measurement. *Meas. Sci. Technol.* **24**, 032001.

VAN OUDHEUSDEN, B. W., SCARANO, F., ROOSENBOOM, E. W. M., CASIMIRI, E. W. F. & SOUVEREIN, L. J. 2007 Evaluation of integral forces and pressure fields from planar velocimetry data for incompressible and compressible flows. *Exp. Fluids* **43**, 153–162.

PERLMAN, E., BURNS, R., LI, Y. & MENEVEAU, C. 2007 *Data Exploration of Turbulence Simulations using a Database Cluster*. Supercomputing SC07, ACM, IEEE.

PERRY, A. E. & CHONG, M. S. 1982 On the mechanism of wall turbulence. *J. Fluid Mech.* **119**, 173–217.

POPE, S. B. 2000 *Turbulent Flows*. Cambridge University Press.

RILEY, J. J., GAD-EL-HAK, M. & METCALFE, R. W. 1988 Compliant coatings. *Annu. Rev. Fluid Mech.* **20**, 393–420.

RODDIER, C. & RODDIER, F. 1987 Interferogram analysis using Fourier transform techniques. *Appl. Opt.* **26** (9), 1668–1673.

RUBINO, E. & LOPPOLO, T. 2016 Young's modulus and loss tangent measurement of polydimethyl-siloxane using an optical lever. *J. Polym. Sci.* B **54**, 747–751.

SALZE, E., BAILLY, C., MARSDEN, O. & JUVE, D. 2015 Investigation of the wall pressure wavenumber-frequency spectrum beneath a turbulent boundary layer with pressure gradient. In *International Symposium on Turbulence and Shear Flow Phenomena, Melbourne, Australia*.

SCARANO, F. 2013 Tomographic PIV: principles and practice. *Meas. Sci. Technol.* **24**, 012001.

SCHARNOWSKI, S., HAIN, R. & KAHLER, C. J. 2012 Reynolds stress estimation up to single-pixel resolution using PIV-measurements. *Exp. Fluids* **52**, 985–1002.

SCHÄFER, L., DIERKSHEIDE, U., KLAAS, M. & SCHRÖDER, W. 2011 Investigation of dissipation elements in a fully developed turbulent channel flow by tomographic particle-image velocimetry. *Phys. Fluids* **23**, 035106.

SCHRIJER, F. F. J. & SCARANO, F. 2008 Effect of predictor-corrector filtering on the stability and spatial resolution of iterative PIV interrogation. *Exp. Fluids* **45**, 927–941.

SCHRÖDER, A., GEISLER, R., ELSINGA, G. E., SCARANO, F. & DIERKSHEIDE, U. 2008 Investigation of a turbulent spot and tripped turbulent boundary layer flow using time-resolved tomographic PIV. *Exp. Fluids* **44**, 305–316.

SCHRÖDER, A., GEISLER, R., STAACK, K., ELSINGA, G. E., SCARANO, F., WIENEKE, B., HENNING, A., POELMA, C. & WESTERWEEL, J. 2011 Eulerian and Lagrangian views of a turbulent boundary layer flow using time-resolved tomographic PIV. *Exp. Fluids* **50**, 1071–1091.

SCHULTZ, M. P. & FLACK, K. A. 2013 Reynolds-number scaling of turbulent channel flow. *Phys. Fluids* **25**, 025104.

SILLERO, J. A., JIMÉNEZ, J. & MOSER, R. D. 2014 Two-point statistics for turbulent boundary layers and channels at Reynolds number up to $\delta^+ \approx 2000$. *Phys. Fluids* **26**, 105109.

SORIA, J. & WILLERT, C. 2012 On measuring the joint probability density function of three-dimensional velocity components in turbulent flows. *Meas. Sci. Technol.* **23**, 065301.

TABATABAI, H., OLIVER, D. E., ROHRBAUGH, J. W. & PAPADOPOULOS, C. 2013 Novel applications of laser Doppler vibration measurements to medical imaging. *Sens. Imag.* **14**, 13–28.

TAKEDA, M., INA, H. & KOBAYASHI, S. 1982 Fourier-transform method of fringe-pattern analysis for computer-based topography and interferometry. *J. Opt. Soc. Am.* **72** (1), 156–160.

TALAPATRA, S. & KATZ, J. 2012 Coherent structures in the inner part of a rough wall channel flow resolved using Holographic PIV. *J. Fluid Mech.* **711**, 161–170.

TALAPATRA, S. & KATZ, J. 2013 Three-dimensional velocity measurements in a roughness sublayer using microscopic digital inline holography and optical index matching. *Meas. Sci. Technol.* **24**, 024004.

TOWNSEND, A. A. 1976 *The Structure of Turbulent Shear Flow*, 2nd edn. Cambridge University Press.

TSUJI, Y., FRANSSON, J. H. M., ALFREDSSON, P. H. & JOHANSSON, A. V. 2007 Pressure statistics and their scaling in high-Reynolds-number turbulent boundary layers. *J. Fluid Mech.* **585**, 1–40.

TSUJI, Y., IMAYAMA, S., SCHLATTER, P., ALFREDSSON, P. H., JOHANSSON, A. V., MARUSIC, I., HUTCHINS, N. & MONTY, J. 2012 Pressure fluctuation in high-Reynolds-number turbulent boundary layer: results from experiments and DNS. *J. Turbul.* **13** (N50), 1–19.

WANG, Z., YEO, K. S. & KHOO, B. C. 2006 On two-dimensional linear waves in Blasius boundary layer over viscoelastic layers. *Eur. J. Mech.* (B/*Fluids*) **25**, 33–58.

WESTERWEEL, J., GEELHOED, P. F. & LINDKEN, R. 2004 Single-pixel resolution ensemble correlation for micro-PIV applications. *Exp. Fluids* **37**, 375–384.

WIENEKE, B. 2008 Volume self-calibration for 3D particle image velocimetry. *Exp. Fluids* **45**, 549–556.

WILLMARTH, W. W. & WOOLDRIDGE, C. E. 1962 Measurements of the fluctuating pressure at the wall beneath a thick turbulent boundary layer. *J. Fluid Mech.* **14** (2), 187–210.

WILLS, J. A. B. 1970 Measurements of the wavenumber/phase velocity spectrum of wall pressure beneath a turbulent boundary layer. *J. Fluid Mech.* **45** (1), 65–90.

WORTH, N. A., NICKELS, T. B. & SWAMINATHAN, N. 2010 A tomographic PIV resolution study based on homogeneous isotropic turbulence DNS data. *Exp. Fluids.* **49**, 637–656.

WU, Y. & CHRISTENSEN, K. T. 2010 Spatial structure of a turbulent boundary layer with irregular surface roughness. *J. Fluid Mech.* **655**, 380–418.

XU, S., REMPFER, D. & LUMLEY, J. 2003 Turbulence over a compliant surface: numerical simulation and analysis. *J. Fluid Mech.* **478**, 11–34.

ZHANG, C., MIORINI, R. & KATZ, J. 2015 Integrating Mach–Zehnder interferometry with TPIV to measure the time-resolved deformation of a compliant wall along with the 3D velocity field in a turbulent channel flow. *Exp. Fluids.* **56**, 203.